Title

Fabrication of a porous anode with continuous linear pores by using unidirectional carbon fibers as sacrificial templates to improve the performance of solid oxide fuel cell

Permalink

https://escholarship.org/uc/item/07f0k2jk

Author

Cheung, Carson

Publication Date

2018

Peer reviewed|Thesis/dissertation

UNIVERSITY OF CALIFORNIA SAN DIEGO

Fabrication of a porous anode with continuous linear pores by using unidirectional carbon fibers
as sacrificial templates to improve the performance of solid oxide fuel cell

A Thesis submitted in partial satisfaction of the requirements
for the degree Master of Science

in

Materials Science and Engineering

by

Carson Cheung

Committee in charge:

Professor Olivia A. Graeve, Chair
Professor Javier E. Garay
Professor Jian Luo

2018

The Thesis of Carson Cheung is approved, and it is acceptable in quality and form for publication on microfilm and electronically:

_____

_____

_____

Chair

University of California San Diego

2018

DEDICATION

I dedicate this thesis to my parents, Esther Cheung and Ken Cheung, for always giving me such loving support, Seongcheol Choi who has been a great mentor through my time in graduate school, and Olivia A. Graeve for this once in a lifetime opportunity to contribute a publication to society.

TABLE OF CONTENTS

LIST OF TABLES

ACKNOWLEDGEMENTS

I would like to acknowledge Professor Olivia A. Graeve for her support and guidance as chair of my committee.

I would also like to acknowledge Seongcheol Choi for his mentorship throughout my graduate life and guidance during the drafting phase of my thesis. He has helped me in an immeasurable way.

Chapter 2, 3, and 4 are currently being prepared for submission for publication of the material. Cheung, Carson; Choi, Seongcheol; Graeve, Olivia A. The thesis author was the primary investigator and author of this material.

ABSTRACT OF THE THESIS

Fabrication of a porous anode with continuous linear pores by using unidirectional carbon fibers as sacrificial templates to improve the performance of solid oxide fuel cell

by

Carson Cheung

Master of Science in Materials Science and Engineering

University of California San Diego, 2018

Professor Olivia A. Graeve, Chair

In order to improve the performance of solid oxide fuel cell (SOFC), both micro-scaled continuous linear pore (CLP) and nano-sized interparticle pore structures were created inside of the NiO-YSZ anode by thermal decomposition of unidirectional carbon fibers in green body during sintering under air atmosphere. A comprehensive analysis of the prepared sample was performed by scanning electron microscopy (SEM), energy dispersive spectroscopy (EDS) mapping, x-ray diffraction (XRD), and thermogravimetric analysis (TGA) to explain how the CLP structure forms during sintering. The CLP structure prepared by this low-cost sacrificial templating method is characterized by its controllable uniform size in microscale and a tortuosity value of 1.003 (coefficient of variation, CV: 0.59). Further discussion proposes that the optimized combination

of the micro-scaled CLP and the nano-sized interparticle pore structures in an anode would be an ideal candidate to maximize the performance of SOFC by maximizing active triple phase boundary sites, minimizing Knudsen diffusion, and improving gas transports.

Chapter 1

Introduction

This chapter details the fundamentals of SOFCs, the fabrication methods of SOFCs, the problems with traditional SOFC anodes, the fabrication methods other researchers have employed to improve the gas transport in SOFC electrodes, and the proposed design of this study to create continuous linear pore structures in the NiO-YSZ SOFC anode to improve gas transport.

1.1 Introduction to fuel cells

Fuel cells are devices that use an electrochemical process to convert gaseous fuels (hydrogen or natural gas) directly into electrical energy. They offer a combination of high chemical to electrical conversion efficiency and low emission gases such as hydrocarbons, sulfur and nitrogen oxides [1]. This is an environmental advantage over modern methods of power generation and makes it a strong candidate for future green energy production. Fuel cells are like batteries by operation and components; they both have an anode, an electrolyte, and a cathode. Furthermore, because fuel cells produce electricity solely from the electrochemical process, they do not have a combustion reaction and are not considered heat engines. Therefore, they are not governed by the Carnot cycle efficiency [2].

1.1.2 Types of fuel cells

As seen in Table 1, there are five main types of fuel cells and they are all characterized by their electrolyte [1, 3, 4]. Because all fuel cells have around the same efficiency, practicality is a major indicator for the usability of a fuel cell. For example, alkaline fuel cells (AFC) require pure hydrogen as fuel because carbon monoxide and carbon dioxide inhibit the alkaline solution electrolyte from catalyzing the electrochemical process. However, pure hydrogen is not easily attained due to problems with hydrogen storage. Similarly, the polymer electrolyte membrane fuel cell (PEM) requires the absence of carbon monoxide and needs an expensive processor to remove them [1]. Phosphoric acid fuel cell (PAFC) is an improvement from the AFC and can function with any hydrocarbons. Molten carbonate fuel cells (MCFC) and solid oxide fuel cells (SOFC) are the most practical due to their ability to directly use commonplace natural gases such as methane for fuel.

Table 1. Types of Fuel Cells [3-5]

Type of Fuel Cell	Electrolyte	Fuel	Oxidant	Efficiency
Alkaline Fuel Cell (AFC)	Potassium hydroxide	Pure hydrogen, or hydrazine liquid methanol	Oxygen/Air	50-55%
Phosphoric Acid Fuel Cell (PAFC)	Phosphoric Acid	Hydrogen from hydrocarbons and alcohol	Oxygen/Air	40-50%
Polymer Electrolyte Membrane Fuel Cell (PEM)	Conducting polymer membrane	Less pure hydrogen from hydrocarbons or methanol	Oxygen/Air	40-50%
Molten Carbonate Fuel Cells	Molten salt such as nitrate, sulphate, carbonates	Hydrogen, carbon monoxide, natural gas, propane, marine diesel	Oxygen/Air	50-60%
Solid Oxide Fuel Cells	Ceramic (example: stabilized zirconia and doped perovskite)	Natural gas or propane	Oxygen/Air	45-60%

1.2.1 The advantages of SOFC

SOFC utilizes a solid ceramic electrolyte and is only operational at temperatures of 750 °C to 1000 °C. The high operating temperature and the ability of the SOFC to use carbon monoxide as fuel allows natural gases like methane to be used as fuel. This can be depicted from the reaction [15]:

$$CH_4 + H_2O \rightarrow CO + 3H_2$$
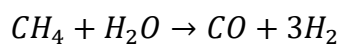
Methane and other hydrocarbon fuels are usually mixed with steam when they are fed into the SOFC. This produces both carbon monoxide and hydrogen gas to be used in the main electrochemical reaction [1-5]:

$$CO + H_2 \rightarrow H_2O + CO_2 + heat$$
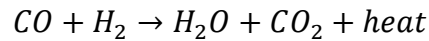
The product water from this reaction can then be recycled to mix with any incoming hydrocarbons. This is tremendously efficient because it eliminates the dangers of carbon monoxide emissions and it allows the SOFC to have useful high-quality heat byproducts for cogeneration. Cogeneration is the production of heating, and cooling along with the production of electricity [6]. Furthermore, SOFC is quiet and vibration-free; this eliminates noise problems usually associated with standard power generation systems [7].

1.2.2 Operations of SOFC

All three components are porous oxide ceramics to allow inlet gases on both sides to flow through the device and permit the electrochemical process to take place. The cell is fabricated by sandwiching a dense ceramic electrolyte between two porous ceramic electrodes. The operation of SOFC begins by heating the cell up to 750 °C to 1000°C [8]. This is the optimal temperature range for typical YSZ electrolyte based SOFC for maximum transport and catalytic activity [9]. Figure 1 depicts the simple case where hydrogen gas and oxygen gas are used as reactants and flowed into the SOFC electrodes. Hydrogen fuel in the anode becomes oxidized into hydrogen ions by the anode material; the hydrogen ions are then transported to the electrochemical reaction sites through a percolating network of anode phases. On the other hand, the oxygen gas in the cathode is reduced and the oxygen ions are transported to the electrolyte through a percolating network of electrolyte phases. Because of the elevated temperatures, the electrolyte has a high enough ionic conductivity

to transport oxygen ions from the cathode to the anode. Oxygen then is finally transported into the anode-electrolyte interface and into the electrochemical reaction sites, where water is formed to complete the electrochemical reaction. This reaction produces heat, water, and electrons. The electrons are then carried from the anode into an external circuit where they are collected.
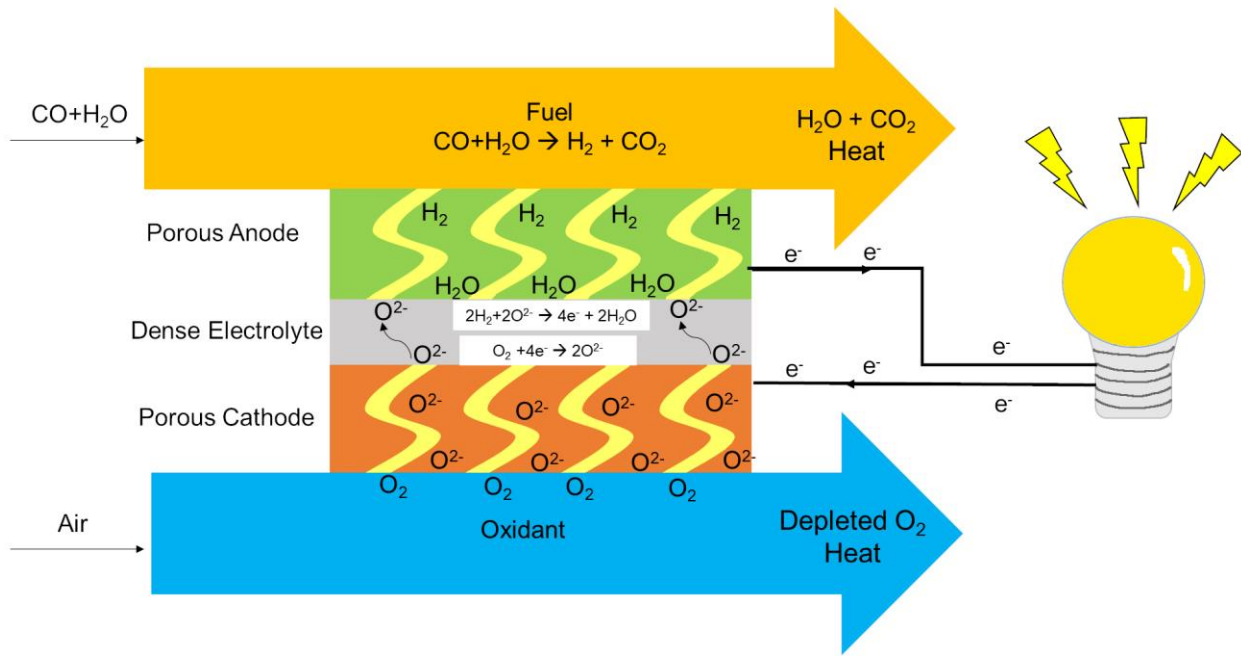
Figure 1. A schematic of an operating SOFC [9].

1.2.3 Electrolyte

Material selection of the electrolyte is critical towards the fabrication of the ideal SOFC. Firstly, the electrolyte needs to be an oxide that has a chemical stability to both reducing and oxidizing atmospheres delivered through the electrodes [10]. Secondly, it must have low electrical conductivity and high density to prevent the loss of generated currents. Most importantly, the electrolyte must have high ionic conductivity for oxygen ion transport [11]. Additionally, a thin thickness electrolyte dramatically increases the ionic transport by decreasing the distance of the

5

ionic path; this feature also decreases the operation temperature [12, 13]. Yttria-stabilized zirconia (YSZ) is the state-of-the-art electrolyte that fulfills all these requirements [8, 11, 14]. Zirconia requires an yttria dopant to maintain the cubic phase. This is necessary because the monoclinic phase dominates at room temperature and the monoclinic phase does not have a high ionic conductivity [10]. Cubic YSZ with 8 mol% yttria is the ideal composition because it yields the highest ionic conductivity and is the lowest concentration needed to stabilize zirconia [11].

1.2.4 Anode

The criteria for an anode are as follow: is electrically conductive, is chemically and thermally stable during fabrication and operation, can catalyze the oxidation of fuels, has the same thermal expansion coefficient as the other SOFC components, has porosity for gas flow, and provides an adequate amount of mechanical strength to act as the mechanical support for the whole SOFC [11, 15]. Ni-YSZ is the most popular candidate in terms of adequately fulfilling all these requirements. Ni-YSZ is a cermet material or composite materials made from sintering ceramics and metals together. This allows the material to have both the hardness and thermal durability of the ceramic, and electrical conductivity of the metal. Furthermore, by forming a cermet, the YSZ decreases the coefficient of thermal expansion (CTE) of the anode [11]. This causes the anode to be even more compatible with the YSZ electrolyte during high-temperature operations.

Addition of YSZ in the anode also increases the amount of oxidation reaction sites in the anode called triple phase boundaries (TPB). Figure 2 shows that the TPB is the interface where Ni, YSZ, and pores meet. The Ni is the electron conduction pathway that delivers electrons out of the anode. The YSZ is the ion conduction pathway that brings oxygen ions to the anodic reaction.

6

The pores are the pathways that transport the hydrogen gas for oxidation. By incorporating YSZ in the anode, the creation of TPBs is not restricted at the anode-electrolyte interface and the YSZ ion conduction pathways extends in to the anode [11, 15].
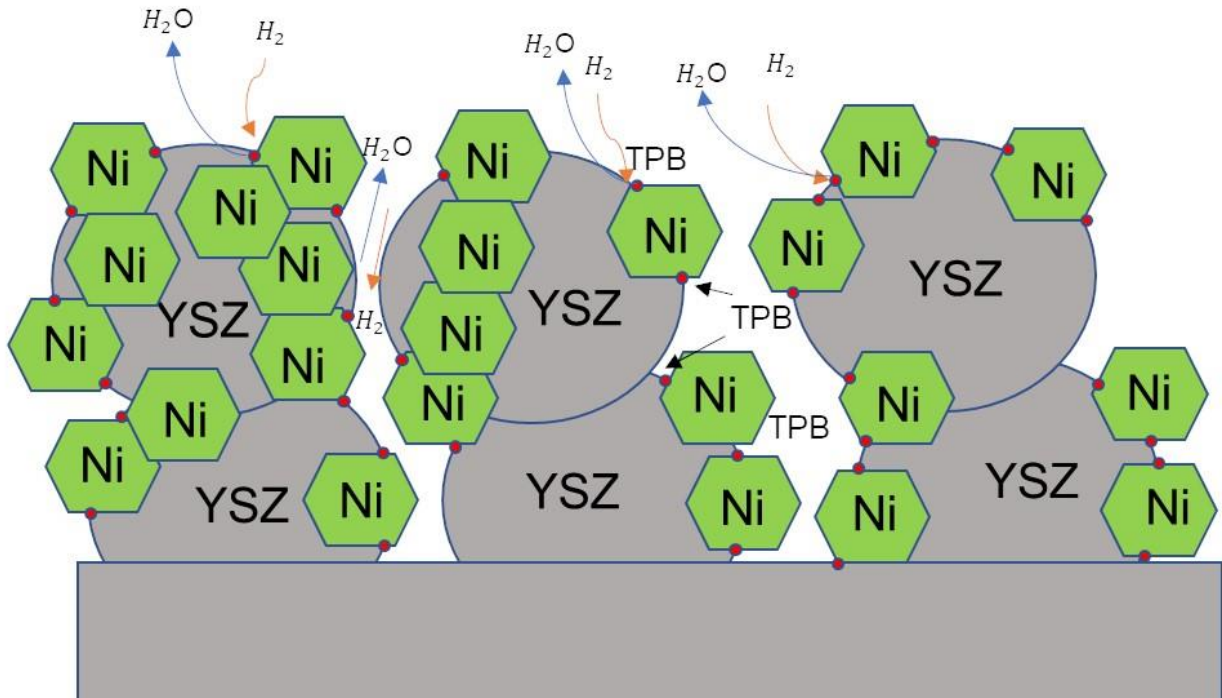
Figure 2. A schematic diagram of Ni-YSZ triple phase boundaries (TPB). The red dots denote the TPB. The white space represents the open pores where hydrogen gas travels through.

1.2.5 Cathode

The criteria for the cathode are like the anode in that it must be porous, electrically conductive and closely match the thermal expansion coefficient of the electrolyte [11, 14]. The cathode also needs to be able to catalyze the reduction of oxygen from the input air. Also, since metals are generally oxidized when exposed to air at high temperatures, a ceramic-based material needs to be selected [11]. Strontium or calcium-doped lanthanum manganite (LaMnO₃) or non-

stoichiometric lanthanum manganite is extensively chosen to fulfill these requirements [11, 14]. Rhombohedral strontium doped lanthanum manganite is the most widely used cathode. It is written as, $La_{1-x}Sr_xMnO_3$, where $0 \leq x \leq 0.5$. The ideal composition of an SOFC component is when x = 0.1 – 0.2; this allows the cathode to have both high electrical conductivity and maintain mechanical and chemical stability with the YSZ electrolyte [11, 14].

1.2.6 Interconnect

Interconnects are used for the electrical contact between the anode of one cell and the cathode of another. This separator acts as a physical barrier that protects the cathode or anode of one cell from the reducing or oxidizing environment, respectively, from the other cell. Because of these requirements, an interconnect needs to withstand both reducing and oxidizing conditions. Doped lanthanum chromite ($LaCrO_3$) is typically selected for its high compatibility with the electrode materials and high electronic conductivity for the accumulation of electricity from all the cells [11].

1.2.7 SOFC stacking configurations

There are two types of SOFC stacking configurations: the planar design and tubular design [9]. For the planar design, cells are made into flat disks rectangular or square plates. The cells are then sandwiched by two interconnects as seen in Figure 3. For the tubular design, as seen in figure 4, the electrodes and the electrolytes are made into long porous tubes. It is configured so that an electrolyte tube is layered on top of one of the electrodes. The other electrode is then layered on top of the electrolyte. Even though tubular designs are favorable for their portability, planar

8

designs are popular for their advantages in power density and ease of fabrication. Furthermore, as depicted in figure 5, SOFC can be electrode-supported or electrolyte-supported SOFC. Electrolyte-supported SOFC has the advantage of being easier to process. However, electrode-supported SOFC are more widely used due to the thinner electrolyte in the design. This provides a lower electrolyte ohmic resistance and allows the SOFC to operate at lower temperatures [9, 11, 12, 14].
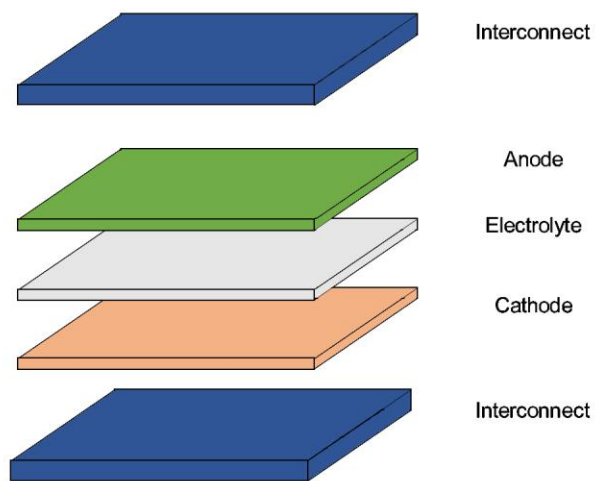
Figure 3. Planar Design of SOFC [9].
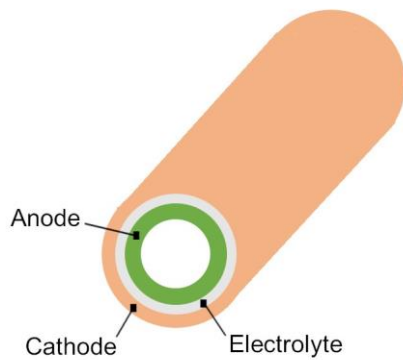
Figure 4. Tubular Design of SOFC [9].
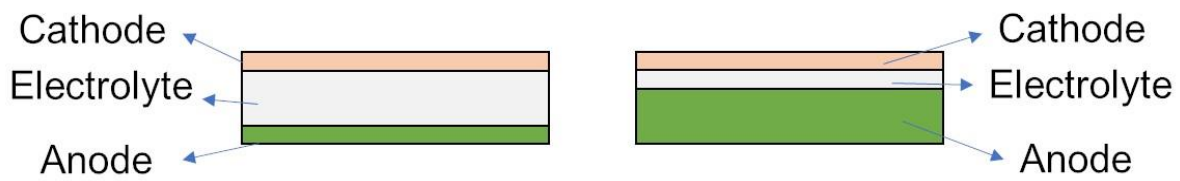
Figure 5. Electrolyte-supported SOFC (left) and electrode-supported SOFC (right) [9].

1.3 Slip casting

Slip casting is the traditional method used for ceramic processing. The ceramic powders can be processed into a slurry or slip by mixing it with water and additives that influence the suspension stability [16]. This slip is then poured into a plaster mold (gypsum mold) that contains a tube- or plate-shaped cavity. Once poured, the slip begins to dry as the water in the slurry is absorbed by the surrounding gypsum mold. This is due to water's capillary action which drives it to travel through the small pores distributed throughout the gypsum mold [17]. As the water escapes, a cast is formed around the inside of the mold walls and the slip dries over time. The green

body is then successfully processed and is detached from the mold. The resulting green body is be sintered to produce the desired SOFC component.

1.4 Slip preparation

The slip or slurry preparation is a crucial step in developing an efficiently molded ceramic. Colloidal stability is the most critical requirement for a quality slip; it is attained with high solid loading and adding dispersants or deflocculants [18, 19]. Colloidal stability is a state in which a solution contains a material or powder that is suspended evenly throughout a liquid medium. However, this stability cannot be achieved unless the interparticle forces between the ceramic particles are altered. This is because, normally when ceramic particles are mixed together in water, immediate agglomeration of the solid ceramics contents occurs [20]. One method to change the interparticle forces is by adjusting the pH and disturbing the electrostatic attractive forces between particles created by a polar liquid [21]. Another method is the incorporation of an additive such as a deflocculant or dispersant [22]. The deflocculant acts as a repulsive barrier between the particles and allow particles to suspend in the slip on their own. Once the particles are evenly separated throughout the slip, colloidal stability is reached. Other additives aside from dispersants are binders and plasticizer; they are added for the improvement of mechanical handling after the green body has casted [17, 23].

1.5.1 Sintering

Sintering is the final process for the fabrication of a solid ceramic component. It is the densification process by which the green particle compacts merge together because of the applied

heat in a high temperature furnace [17]. It also decreases the amount of porosity. The mechanisms that drive this process are surface diffusion and viscous flow; the driving force for both mechanisms is the decrease in surface energy [24, 25]. There are three stages of sintering. The "initial stage" is when the particles attain enough mobility to orient themselves in a way that increases the number of points of contact between each other. As a result, bonds between particles begin to form and necking initiates [17, 25]. The "second stage" or "intermediate stage" is the onset of pore elimination and grain growth. Grain is the name given to the crystalline particles after sintering has started. At this stage, a 3D network of continuously merged particles and 5-10% porosity is left [25]. During the "final stage", the remaining pores are eliminated as the grains finish growing.

1.5.2 Pore forming agents (PFA) and carbon fiber

The addition of pore-forming agents (PFA) to slips has become a popular procedure for the fabrication and tuning of pores in ceramics. This is done by first incorporating the PFA either by dispersing and mixing PFA powders during the slip preparation or by processing it into the green body during the shaping/casting phase [26]. Then, the PFAs undergo pyrolysis during the initial sintering step, where the ceramic particles begin to sinter around the PFAs and generate pores with shapes identical to that of the PFAs [27]. Because it requires a lot more surface energy to stimulate enough densification to close off the large PFA-shaped voids, they are retained throughout the rest of the sintering process [27]. Organic and pure carbon powders, such as polyethylene and graphite, are primary candidates to act as PFAs [26, 27]. This is due to their rigidity in their shapes and adequately low pyrolysis temperatures.

12

Sharing similar chemical properties as graphite, carbon fiber is a quality candidate as a PFA [28]. It is seen in table 2 that it can have a diameter of between 5-11 μm, a substantially high Young's modulus, and low thermal expansion. Tranchard et al. reported that carbon fiber begins to decompose at the temperature range of 400-500 °C [29]. Carbon fibers can be processed into tows, tapes, and even fabrics depending on the application [28]. For this study, unidirectional carbon fiber fabric will be the PFA because it is composed of a two-dimensional array of carbon fibers with the same orientation.

Table 2. Properties of carbon fibers made from different precursors [28]

Properties, units	Precursors		
	PAN	Pitch	Rayon
Fiber diameter, μm	5 – 8	10 - 11	6.5
Young's Modulus, GPa	230 – 595	170 - 980	415 - 550
Coefficient of thermal expansion			
Axial, 10^{-6} m/°C	-0.75 to -0.4	-1.6 to -0.9	-
Transverse, 10^{-6} /°C	7 – 10	7.8	-

1.6.1 Scanning electron microscopy Scanning electron microscopy (SEM) is one of the best characterization techniques for the imaging of the surface of microstructures. It has the same basic methodology as optical microscopy; a beam of a certain wavelength is discharged on a sample, the sample is then magnified by lenses, and consequently imaged [30]. The difference is SEM utilizes an electron beam instead of a light source and electromagnetic lenses instead of optical lenses. This is because of the resolution limit set by the wavelength of light (400 nm); a

wavelength that cannot resolve images less than 220 nm [30]. A 100-kV electron beam has a much smaller wavelength (0.037 angstroms) and can image details in the nanometer range. The electron beam is focused through a series of electromagnetic lenses which have scattering interactions with the sample. By using a series of electron scattering detectors, an image on a computer can be rendered according to where the detectors are hit.

1.6.2 Energy dispersive X-ray spectroscopy (EDS)

Energy Dispersive X-ray Spectroscopy (EDS) is a technique used to analyze elemental composition. The Rutherford-Bohr model of the atom governs that at ground state, the number of orbitals closest to the nucleus are filled according to the number of protons (denoted Z) [31]. Orbitals closest to the nucleus are first filled; once one inner shell is filled, a shell orbiting that shell is then filled. When an electron probe collides with one of these orbital electrons, it gets scattered out of the ground state orbital, excites to a higher orbital shell, and produces a vacancy in the inner orbit. An x-ray is released when the excited electron relaxes back to their original ground state shell [31]. The x-ray energies emitted are different for each Z element because they each have distinctive amounts of electron orbital levels filled. With the implementation of a pulse height analyzer, these energies can be detected, characterized, and matched to their respective elements.

1.6.3 X-ray diffraction (XRD)

X-ray Diffraction is a technique used to characterize the composition and crystal structure of crystalline materials. Crystalline materials each have different crystal structures and each

crystal structure have a distinct set of Miller indices [32]. Miller indices are the reciprocal integers that detail a set of planes that are unique to each specific crystal structure. Furthermore, each crystal structure has a set of interplanar distance called d-spacing. Using d-spacing, the XRD can characterize the composition of different crystal structures in a certain sample. When an x-ray is directed towards a sample, multiple beams strike the sample and scatter at certain angles. If two beams scatter at the same angle, a constructive interference between the two x-rays is exhibited and Bragg's law is satisfied. Bragg's law can be described in the equation [32]:

$$2dsin(\theta) = n\lambda$$

This equation illustrates that there exists a characteristic plane with interplanar distance d which scatters the x-rays at an angle θ. When the x-rays are scattered in a way that causes the two beams to behave constructively, no matter what magnitude n of the radiation wavelength λ, the Bragg's condition is satisfied. The XRD uses this principle to analyze the crystal structure and composition of a crystalline sample.

1.6.4 Thermogravimetric analysis

TGA is an analytical technique used to determine the change in mass by the effects of temperature change. It utilizes a dual component device called a thermo-balance; a device that has both an analytical scale and a furnace. Samples are put into the machine and temperature parameters, such as heating rate and holding temperature, are inputted into the system [33]. The type of atmosphere can also be changed to either inert gases, like nitrogen, argon and helium, or reactive gases, like oxygen, hydrogen, and carbon dioxide. During heating or cooling, the TGA

keeps track of the mass loss or gain and records it on a plot. Once the run is over, an integral curve is plotted to analyze trends such as mass versus temperature and mass versus time.

1.7.1 Electrochemistry and overpotential of SOFC

Overpotentials, or polarizations, in the SOFCs electrochemistry are losses in voltage caused by deficiencies in the design, material, or microstructure of the SOFC components. They are closely analyzed to determine the final cell potential of an operating fuel cell. The three activation potentials are: activation overpotential, ohmic overpotential, and concentration overpotential [4, 34].

1.7.2 Electrochemical reactions, triple Phase Boundary, and activation overpotential

To fully model the activation overpotential and electrochemical process of SOFC, it is important to consider the transfer of chemical species and charge transfer that occur at the electrodes. The following equations detail the ion transfer and oxidation reaction that facilitate the anode's charge transfer process [4, 34]:

1) Overall Equation:

$$H_2 + O^{2-} \Longleftrightarrow H_2O + 2e^- \quad (Step\ 1)$$
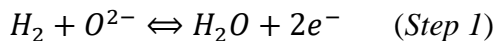
2) Adsorption/chemisorption of hydrogen at anode surface:

$$H_2(bulk) + (anode, surface) + (anode, surface) \Longleftrightarrow H(anode, surface) +$$

$$H(anode, surface) \quad (Step\ 2)$$

16
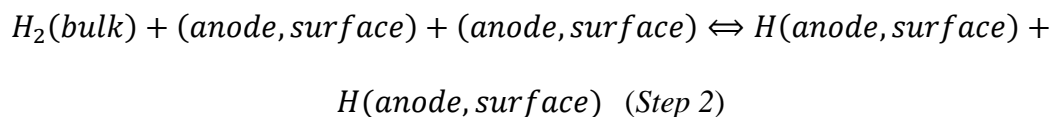
3) Ion and electron transfer at Triple Phase Boundary (TPB):

$$H(anode, TPB) + O^{2-}(electrolyte, TPB) \Longleftrightarrow (anode, TPB) + OH^-(electrolyte, TPB) +$$

$$e^-(anode, TPB) \qquad (Step\ 3)$$

$$H(anode, TPB) + OH^-(electrolyte, TPB) \Longleftrightarrow (anode, TPB) + H_2O(electrolyte, TPB) +$$

$$e^-(anode, TPB) \qquad (Step\ 4)$$
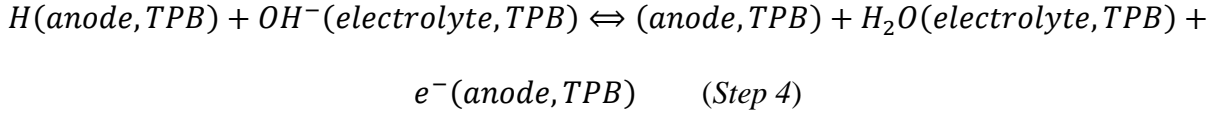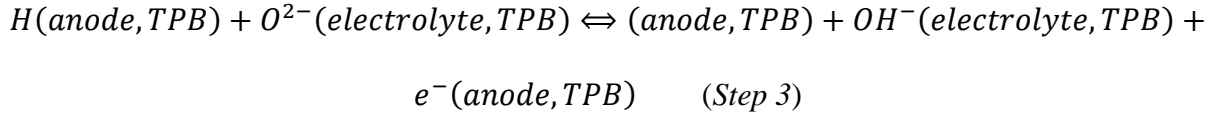
4) Adsorption/Desorption of H₂O on YSZ surface:

$$H_2O(electrolyte, TPB) \Longleftrightarrow H_2O + (electrolyte, TPB) \qquad (Step\ 5)$$
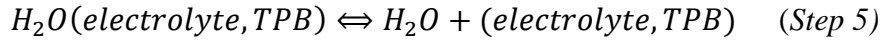
5) Oxygen ion diffusion from surface to bulk YSZ:

$$V_O^{**}(electrolyte, bulk) + O^{2-}(electrolyte, TPB) \Longleftrightarrow (electrolyte, TPB) +$$

$$O_O^x(electrolyte, bulk) \qquad (Step\ 6)$$
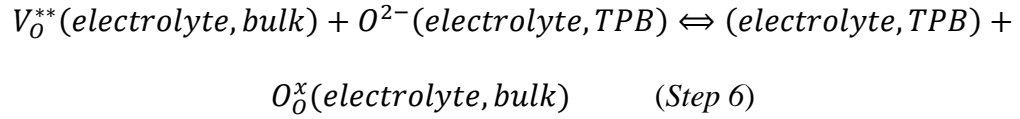
Like the oxidation of H_2, the oxygen reduction process also requires a multi-step mechanism [4, 34]:

1) Overall Equation:

$$\frac{1}{2}O_2 + V_O^{**}(electrolyte, bulk) + 2e^- \Longleftrightarrow O_O^x(electrolyte, bulk) \quad (Step\ 7)$$
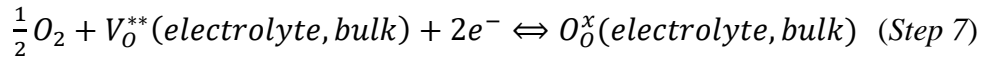
2) Adsorption/chemisorption of oxygen at cathode surface:

$$O_2 + (cathode) + (cathode) \Longleftrightarrow O(cathode) + O(cathode) \qquad (Step\ 8)$$
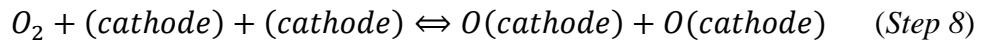
3) Diffusion of oxygen ions to TPB:

$$O(cathode, surface) \Longleftrightarrow O(cathode, TPB) \qquad (Step\ 9)$$

$$O(cathode, TPB) \Longleftrightarrow O(electrolyte, TPB) \qquad (Step\ 10)$$
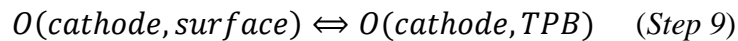
4) Diffusion of oxygen ions from TPB to electrolyte bulk

$$O(TPB) + V_O^{**}(electrolyte, bulk) \Longleftrightarrow O_O^x(electrolyte, bulk) + (TPB) \quad (Step\ 11)$$
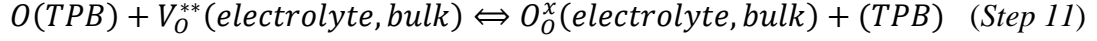
The notations in parenthesis denote the surface on which certain species are attached to. *O(TPB)* represents an oxygen atom attached to the TPB, whereas *(TPB)* represents an empty TPB site. $V_O^{**}(electrolyte)$ denotes an oxygen vacancy on the electrolyte surface and $O_O^x(electrolyte, bulk)$ denotes a lattice oxygen in the electrolyte.

Activation over-potential is the energy required to catalyze the charge transfer process. It is also the amount of additional potential needed to drive the electrochemical process past the equilibrium to allow current to start flowing. According to Zhu et al. and Bessler et al., step 4 is the rate determining step. Taking this into consideration, the activation potential current density takes on the form of:

$$i = i_0 \left[\exp\left(\alpha_a \frac{n_e F \eta_{act}}{RT} \right) - \exp\left(-\alpha_c \frac{n_e F \eta_{act}}{RT} \right) \right]$$

i_0 is the exchange current density; it is a function of species concentration, which depends on the temperature and chemical composition [4]. α_a and α_c are charge transfer coefficients and follow the relation: $\alpha_a + \alpha_c = 1$. α is the degree of symmetry exhibited the activation barrier; a symmetric reaction yields $\alpha = 0.5$ [44]. n_e is the number of electrons. F is Faraday's constant. η_{act} is the activation potential.

1.7.3 Ohmic overpotential

The Ohmic overpotential is the ionic resistance of the electrolyte material. With respect to current density, this overpotential can be expressed as: $\eta_{ohm} = i R_{tot}$. η_{ohm} is the ohmic

overpotential, i is the current density and R_{tot} is the total cell resistance. R_{tot} is composed of all the resistances from each individual cell component [34]:

$$R_{tot} = \rho_e l_e + \rho_a l_a + \rho_c l_c + R_{contact}$$

ρ_e, ρ_a, and ρ_c are specific electrical resistance of the electrolyte, anode, and cathode respectively. l l_e, l_a, and l_p are the thickness of the electrolyte, anode, and cathode respectively. $R_{contact}$ is the resistance of any contact in the system and depends on the quality of adherence between the anode and the electrolyte.

1.7.4 Concentration overpotential

Concentration overpotential or mass potential loss is a result of the reactant concentration changes that occur at the electrode/electrolyte interface. Changes in concentration at the interface are caused by the increased conversion of the reactants into products. Therefore, the concentration loss is attributed to the gas concentration difference between the electrode surface and the electrode/electrolyte interface [4]. This interface can be called the catalytic because it is the area where TPB reaction sites are prominent. This overpotential is dictated by the porosity and microstructure of the electrode. According to Chen et al. and assuming equimolar counter diffusion and H_2 as fuel, the concentration overpotential can be expressed as [4]:

$$\eta_{conc,a} = -\frac{RT}{2F} \ln \left[\frac{1 - \left(\frac{RT}{2F}\right)\left(\frac{l_a}{D_e p^I_{H_2}}\right)i}{1 + \left(\frac{RT}{2F}\right)\left(\frac{l_a}{D_e p^I_{H_2O}}\right)i} \right],$$

19

$$\eta_{conc,c} = -\frac{RT}{4F} \ln \left\{ \frac{\left[\left(\frac{p_c}{\delta_{O_2}} \right) - \left(\left(\frac{p_c}{\delta_{O_2}} \right) - p_{O_2}^I \right) \right] \exp \left[\left(\frac{RT}{4F} \right) \left(\frac{\delta_{O_2} l_c}{D_e p_c} \right) i \right]}{p_{O_2}^i} \right\}$$

Here, D_e is the effective diffusion coefficient, p_i^I is the partial pressure of the gaseous chemical species at the inlet, p_a is the partial pressure in the anode, p_c is the partial pressure in the cathode, δ_i is the l_a and l_c are the thickness of anode and cathode, respectively. D_e is formulated as:

$$D_e = \frac{\varepsilon}{\tau^2} D_{bulk}$$

ε represents the porosity of the system, τ is the tortuosity of the system, τ^2 is the tortuosity factor and D_{bulk} is the bulk diffusion coefficient of the inlet gas [35]. Tortuosity in porous structures is depicted in figure 6 and can be derived as [36]:

$$\tau = \frac{\Delta l}{\Delta x}$$

Therefore, the tortuosity of a system can be defined as the degree of directness between two points. The amount of current density produced during an operating fuel cell at steady-state is formulated as [37]:

$$j = \frac{nFD_e(c_R^* - c_R^0)}{\delta}$$

In this equation, n is the number of electrons, F is the Faraday constant, δ is the thickness of the electrode, c_R^* n is the concentration of reactants at the reaction interface, and c_R^0 is the concentration of reactants in the bulk gas at the electrode surface. This equation indicates that an increase in current density requires a larger concentration of reactants and an increase in gas pressure. An

alternative to this is by decreasing D_e. This can be done by either increasing the porosity or decreasing the tortuosity of the porous system. The main goal of this thesis is to focus on decreasing the tortuosity parameter by creating direct linear pathways for the inlet gas.
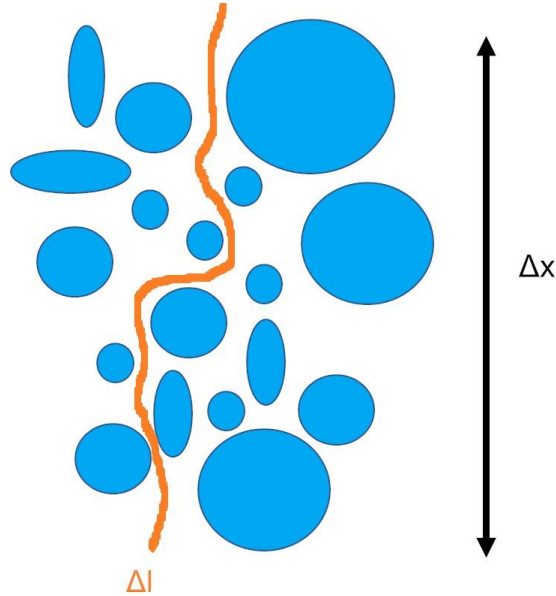
Figure 6. Schematic for the derivation of tortuosity.

1.7.5 Overall cell potential and Nernst potential

The overall cell potential or operating potential of the cell is a result of the culminated differences of the above overpotential losses that occur in different parts of the fuel cell. This final potential can be written as a function of local density current *i* [4]:

$$E_{cell} = E_{rev} - \eta_a(i) - |\eta_c(i)| - \eta_{ohm}(i) - \eta_{conc}(i)$$

In this equation the η_a, η_c, η_{ohm}, and η_{conc} are the variables for anode activation loss, cathode activation loss, Ohmic overpotential, and concentration overpotential. E_{rev} is called the Nernst

21

potential or open circuit voltage. This is the maximum possible potential which the cell can produce operating reversibly. In the case of hydrogen oxidation, the Nernst potential can be calculated using the Nernst equation [4]:

$$E_{rev} = E^0 + \frac{RT}{2F} \ln \left(\frac{p_{H_2,a} p_{O_2,c}^{\frac{1}{2}}}{p_{H_2O,a}} \right)$$

1.8.1 Gas inefficiencies of standard SOFC electrode pores

As seen in figure 7, the pore morphology of a traditional SOFC anode is not controlled and consists of a percolation of disordered interparticle pore channels. This causes the distance taken by the gases to be tortuous or distorted from the ideal. In addition, within the interparticle pore channels of the traditional SOFC anode are some areas with nano-sized pores that have high specific surface area and play a crucial role to maximize the catalytic activity at TPB sites. However, the movement behavior of the gas molecules, which are traveling through a relatively long narrow channel with diameter between 2 to 50 nm, follows Knudsen diffusion [38, 39]. In this phenomenon, the gas molecules are confined in a narrow channel because the gas molecules collide with the narrow pore walls much more frequently than with each other; this results in an increase in the mean free path of the gas molecules. Thus, any areas where the size of the interparticle pores in an anode is between 2 to 50 nm are, in fact, a bottleneck of gas transport of H_2 and steam during operation of SOFC. Because of this reason, an anode with only nano-sized interparticle pores has performance limitation.
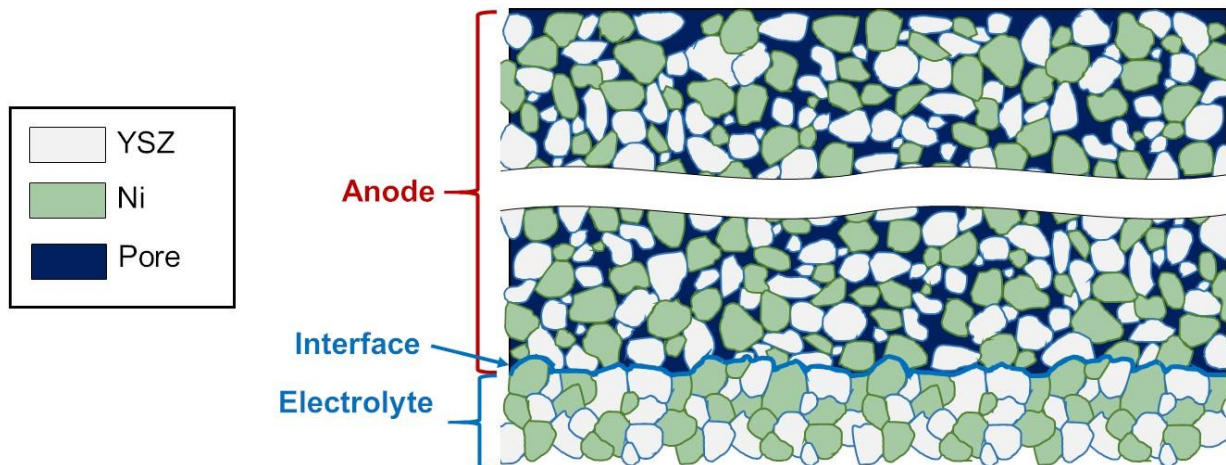
Figure 7. Pore morphology of a traditional NiO-YSZ anode.

1.8.2 Pore Engineering to improve gas transport

Substantial literatures have demonstrated that the fabrication of anodes with pores structures that have low tortuosity and an orientation perpendicular to the inlet surface significantly improve the power density of the SOFC. Pan et al. constructed and analyzed an SOFC with small increments of cylindrical pores dispersed throughout the anode substrate [40]. The disconnected cylindrical pores were formed using "paper-fibers" that was prepared using ash-free filter paper in distilled water. Three Ni-YSZ anode pellet samples were prepared, and each had semi-cylindrical pores dispersed within with different alignment orientations. Pan et al. then analyzed the maximum power density of the three samples; the pores that were oriented parallel to the gas flow produced the highest power density.

Yoon et al. tested the performance of an anode with conical pores of 225 µm in diameter [41]. The pores were "micromachined" by using laser ablation and were orderly oriented parallel to the thickness direction or gas flow direction. For analysis, they produced a baseline cell with

23

random porosity and three micromachined cells. Each micromachined cells are distinguished by the distance of the gap between the bottom of the pore channel and the electrolyte: 150 μm, 230 μm, and 250 μm. A j-v characteristic (current vs voltage) curve of the micromachined cells and a baseline cell was then plotted for analysis. It is confirmed that the current density is significantly greater for the micromachined cells than the baseline cells. Furthermore, SOFC performance increased as the gap distance between pore channel and electrolyte decreased.

Chen et al. fabricated an anode substrate with long shard like porous structures that exhibited low tortuosity [42]. The porous structures were developed using a freeze tape casting method. It is a method where a tape-casted green body is immediately freeze-dried to form desired porous shapes in the green structure. The current, voltage, and power density analysis demonstrated that the anode with the shard-like pores had two times the amount of power density than that of a normal tape-casted anode. Furthermore, the tortuosity factor was determined to be at a minimum value of 1.3 [42]. Whereas, traditional anodes typically have a value of 1.5 and 4 [43].

1.9.1 Thesis proposal: Fabricate continuous linear pores in anode to maximize gas transport

This thesis will focus primarily on the fabrication of linear pores in the anode. To fully minimize the distance between the electrolyte and the outer surface of the anode, the linear pores need to be parallel to the thickness direction of the electrode. As seen in figure 8, the linear pores create a path directly to the electrode-electrolyte interface. An ideal pore system should consist of a distribution of nanoscale interparticle pores and microscale continuous linear pores that are well

dispersed in the electrodes, have a uniform diameter, and are perpendicular to the inlet surface of electrodes [44]. The tortuosity value of ideal linearity of CLP is 1, which means that the linear pores are perfectly perpendicular to the inlet surface of electrodes. Most of electrochemical reaction occur at TPBs in the nanoscale interparticle pore because of their high specific surface area [45, 46]. Although there are also electrochemical reactions at the TPBs on the surface of CLP, the major role of CLP is to facilitate the mass transport of hydrogen gas molecules and generated steam at TPBs in an anode to maximize the reaction rate at the active TPBs on the overall system. Moreover, the microscale characteristic of the CLP further improves mass transport by preventing Knudsen diffusion [38, 39].
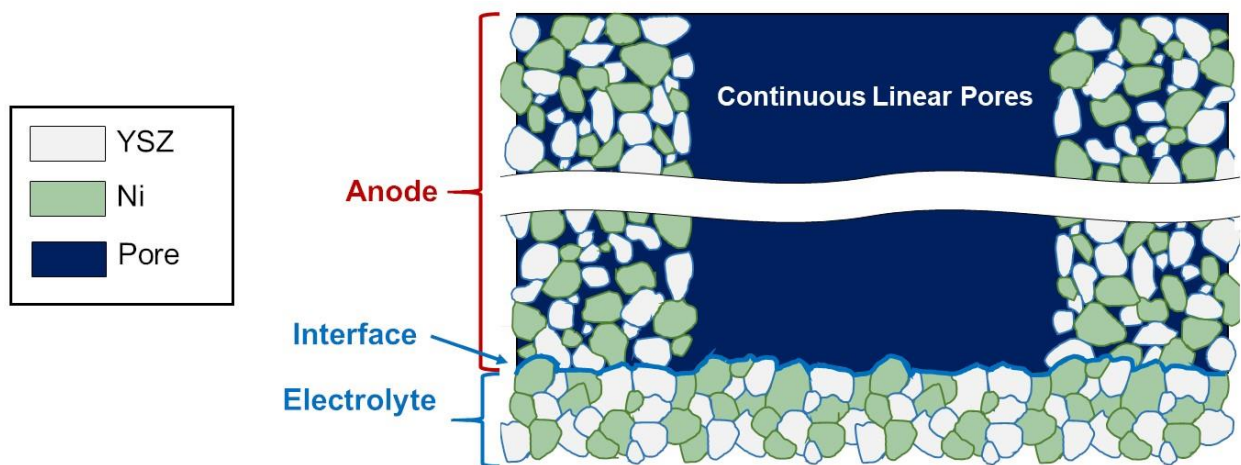
Figure 8. NiO-YSZ with both a random distribution of interparticle pores and CLP.

1.9.2 Statement of research

It is proposed that the fabrication of a NiO-YSZ with pore structures with continuous linear pore structures (CLP) oriented perpendicular to the inlet of the surface and interparticle pores can be made by using slip casting with unidirectional carbon fibers as sacrificial template. The

complete thermal decomposition of unidirectional carbon fibers during sintering leaves CLP with uniform shape and size and has a tortuosity value that is very close to the ideal value of 1. To better understand the formation of the CLP in an anode during thermal decomposition, morphology, elemental analysis, crystal structure, and thermogravimetric analysis of the CLP are investigated. Further discussion will talk about the potential effects of the CLP during SOFC operation in terms of active TPBs, Knudsen diffusion, and gas transport trends.

Chapter 2

Experimentals

2.1 Preparation of a disc-shaped NiO-YSZ anode with a CLP structure

Figure 9 depicts the whole procedure of the fabrication of a NiO-YSZ anode with a CLP structure. In order to facilitate unidirectional carbon fiber bundles as a sacrificial template and hold their perpendicular configuration inside of the green body, we created an assembly mold of a disk-shaped silicone and a plaster. The role of the disk-shaped silicone is to strongly keep the configuration of the unidirectional carbon fiber bundles perpendicular to the top surface of the green body. Thus, we used silica-reinforced silicone rubber with hardness of shore 40A because it does not deform and is strong enough to hold unidirectional carbon fiber bundles during the whole procedure. And, the plaster around the mold assembly absorbs all the water out of the slip during slip casting.

Figure 9. Schematic procedure of a disc-shaped NiO-YSZ anode with a continuous linear pore structure.

First, to prepare a disk-shaped silicone with a diameter of 1.9 cm and a height of 1.27 cm, 20 mL of precipitated-silica reinforced polydimethylsiloxane (PDMS, TS141, Grace Continental Korea Co., Ltd) and 1 wt% of 2,5-bis(tert-butylperoxy)-2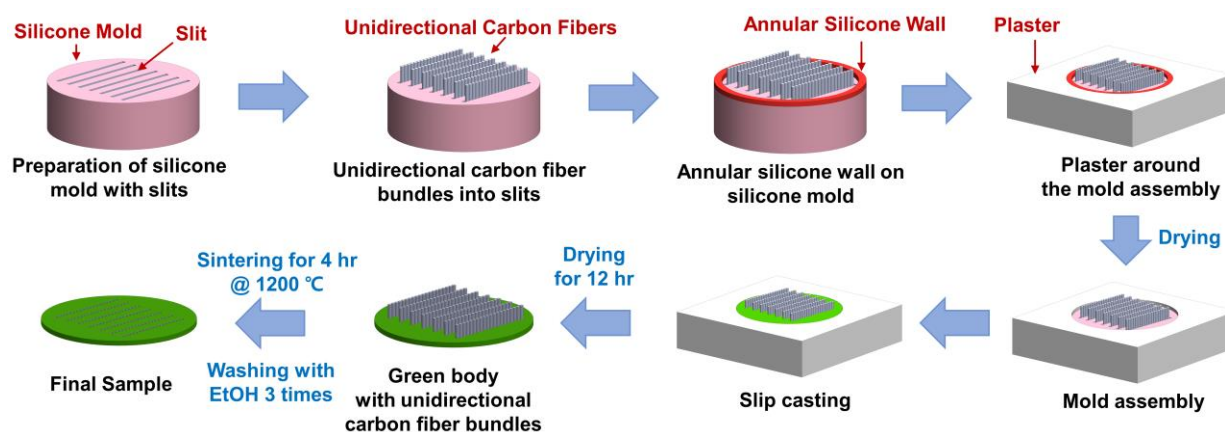,5-dimethylhexane, known as a peroxide curing agent (Luperox®, technical grade of 90%, Sigma-Aldrich) is mixed for a while, placed into a metal mold, and then cured under pressure at 200 ℃ for 20 min [47]. Second, parallel slits with dimensions of 0.75 cm x 0.005 cm x 1 cm are created in the middle of the disk mold. Third, the unidirectional carbon fiber bundles (CF31x, The Composite Store, Tehachapi) are tightly inserted into these slits. Forth, an annular silicone wall (prepared in the same way as the disk-shaped silicone mold) with a diameter of 1.9 cm and a thickness of 0.2 cm is placed on the edge of the top surface of the disk-typed silicone mold. Fifth, the silicone mold with unidirectional carbon fibers and an annular silicone wall is placed in the center of a wooden mold, and plaster mixture of 1:1 ratio of calcium sulfate dihydrate, known as plaster (gypsum, Plaster of Paris, Craft Smart) and water was poured into the wooden mold. After the plaster is completely dried, the mold assembly is finally prepared by releasing the assembly from the wooden mold and removing the annular silicone wall from that assembly.

To prepare the slip, 20 g of NiO-YSZ powder (60 wt% NiO, 40 wt% of 8 mol% yttrium-stabilized zirconia (Surface Area: 1-4 m^2/g, Nexceris) and 3 mL of deionized water are mixed for 30 min. And, then 50 mg of poly(acrylic acid) water solution (Duramax D-3005, Rohm & Haas) as a dispersant is added into the mixture and stirred for 1 hr. Simultaneously, 0.2 g of poly(vinyl alcohol) (PVA, M_w: 13k-23k, 98 % hydrolyzed, Sigma Aldrich) as a binder is mixed with 3 mL of deionized water at 80 ℃ to produce a binder solution [48, 49]. Once dissolved, it is cooled down to room temperature and added into the slip mixture. The slip is then stirred for 4 hours. Then, this

NiO-YSZ slip is casted into the cavity of the mold assembly until the whole cavity is filled. Once the cavity is filled, the slip is left to dry for 12 hr. After that, the green body is removed from the mold assembly and sintered at 1200 °C (heating rate of 5 ℃/min) under air atmosphere in a furnace for 4 hours [50, 51].

2.2 Characterization

All the characterizations in this study were done on NiO-YSZ. We do not cover a reduced porous anode in this study. Scanning electron microscopy (SEM, FEI Quanta™ FEG 250, Thermo Fisher Scientific™) was performed at the accelerated voltage of 10 kV to image the morphologies of all the samples without any sputter coating. To visualize the cross-sectioned continuous linear pores of the samples, each sample was fractured through the cross-sectional plane where the linear pores are fabricated. The mean diameter, the size distribution, and tortuosity value of the CLPs of the final sample were determined from the 300 CLPs of the acquired SEM images. Tortuosity is determined by measuring the thickness of the sample and using it as a reference for the shortest distance between the top and bottom surfaces. Then, the length of each CLP is measured along its midpoint and then the ratio between the pore length and the reference distance is calculated to determine the tortuosity value. Energy-dispersive x-ray spectroscopy (EDS) mapping was conducted at 20 kV on the top surface and the cross-section of the CLP of the sample to determine the elemental phases NiO-YSZ and the TPB sites. X-ray diffraction (D2 PHASER, Bruker) with Copper K_α of 1.5418 Å was performed on the raw unidirectional carbon fiber fabric, the mixture of NiO-YSZ powders, and the sintered NiO-YSZ to verify whether the final sample contains any carbon sources inside. Thermogravimetric analysis (TGA, SDT Q600, TA Instruments) was used to analyze the thermal decomposition behavior of carbon fibers in the green body of Ni-YSZ

during sintering at a temperature of 1200 ℃ with a heating rate of 5 ℃/min and under air atmosphere with an air flow rate of 300 mL/min.

Chapter 2, 3, and 4 are currently being prepared for submission for publication of the material. Cheung, Carson; Choi, Seongcheol; Graeve, Olivia A. The thesis author was the primary investigator and author of this material.

Chapter 3

Results and discussion

3.1.1 Morphology of CLPs

As shown in figure 10 a), the cross-sectioned SEM image shows that the CLPs have been successfully constructed in an NiO-YSZ planar anode by using unidirectional carbon fiber bundles as a sacrificial template after sintering. As a reference for discussion, the smooth surface is the top surface which will be the anode-electrolyte interface and the rough surface is the bottom surface where the inlet hydrogen gas will enter. The length of the CLPs in figure 10 a) stretches from the top surface to the bottom surface and all CLPs are perpendicular to the surface. Figure 10 b) presents the top surface view of the pores of the anode. Each circular-shaped hole is an entrance at the surface and is a result of the thorough penetration of the carbon fibers through the anode. The SEM image of Figure 10 c) depicts one of the circular entrances on the surface of the anode; the mean diameter of these entrances is 7.4 µm (CV: 22.97). Furthermore, it also shows well-dispersed interparticle pores throughout the sample. Some interparticle pores are on the edge of the linear pore; this gives proof that the linear pores combine with the interparticle pore system. Figure 10 d) depicts a side view of linear pores near the bottom surface; the linear pores are considerably defined. Figure 10 e) presents the side view of the continuous linear pores a high magnification at 15k. This SEM image also shows that the interparticle pores are well-distributed throughout the wall of the CLPs. the mean diameter of the linear pores at the side view is 6.9 µm (CV: 11.35). The linear pore does not show any sign of discontinuity and validates that the whole linear pore structure is continuous. Furthermore, interparticle pores are dispersed throughout the sample; this gives evidence that the sintering parameters are successful in creating interparticle

pores. Also, there are interparticle pores on the inner walls of the linear pores; this adds further proof that the linear pores combine with the interparticle pore system. It is clear from these findings that the linear pores are continuous pathways from the top surface to the bottom surface. Also, it is evident that these continuous pathways connect with the interparticle pore system.
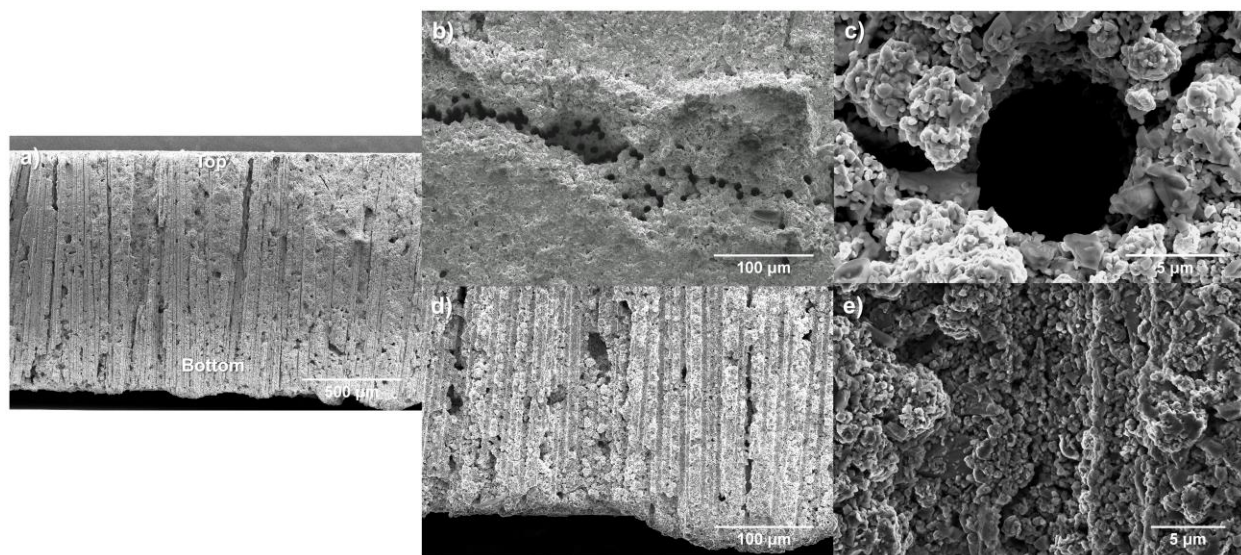
Figure 10. Scanning electron microscopy images of a porous NiO-YSZ anode with continuous linear pores: a) cross-section at 200x, b) top surface at 1k, c) top surface at 10k, d) cross-section at 1k, and e) cross-section at 15k magnification.

One of the most phenomenal result of the CLP structure of the anode is the achievement of an ideal average tortuosity of 1.003 with very low CV value of 0.59 as plotted in figure 11. A normal distribution curve of the tortuosity because the median and mode are very close to the mean; the median is 1.003 and the mode is 1.002. Traditional anodes typically have a tortuosity value between 1.25 and 2 [52-54]. Therefore, it is concluded that all the CLPs in our sample have

produced the shortest continuous path from the top surface to the bottom surface. This is paramount when compared to traditional SOFC electrodes because during SOFC operation at 800 ℃, very low tortuosity would result in the most efficient gas transport for both hydrogen gas from inlet and produced steam at TPBs of anodes.
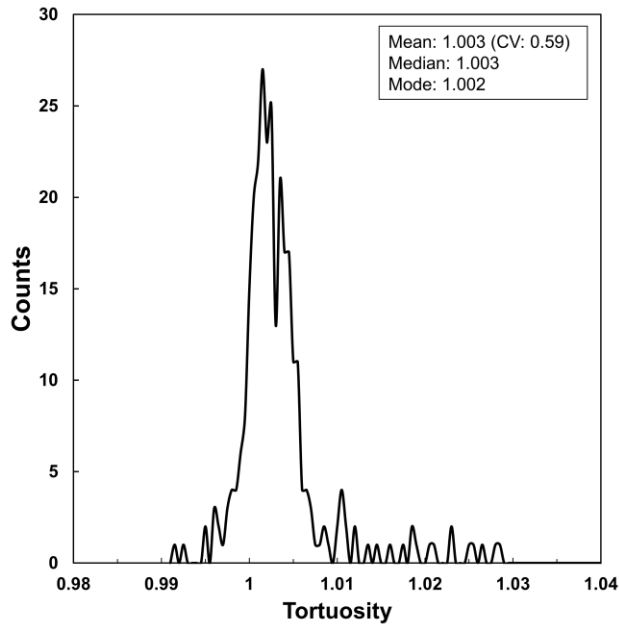
Figure 11. Distribution of tortuosity values of continuous linear pores in NiO-YSZ.

Figures 12 a) and b) show the morphology the carbon fibers we used at different magnifications at 1k and 20k, respectively. The surface of the carbon fibers is free from residue and deformities despite not having a washing procedure; this suggests that the carbon fibers we used is a good sacrificial template without any further treatments. The mean diameter of the carbon fibers is 7.9 µm (CV: 8.78) from SEM images. By comparing figures 10 c) and e) to figures 12 a) and b), respectively, it is clear to see that the shape of the linear pores resembles the shape of the carbon fibers. The figure 12 is the diameter distribution of unidirectional carbon fiber bundles,

CLPs at top/bottom surface of the sample, and CLP in the cross-sectioned sample from SEM images. Table 3 shows the quantification for the central tendency of the distribution plots. The mean, median, and mode for all plots are significantly close to each other. This suggests that all distribution plots have a normal distribution and the CV is an accurate indicator for the uniformity of the diameters. The mean diameters of the entrance points have more variation than the mean diameters measured from the side view of the linear pores because the top surface is not completely flat. The uneven surface distorts the true cross-sectional shape of the linear pore and produces variations in the measurement. The mean diameters measured at the top and at the side are considerably close to the mean diameter of the carbon fibers. Moreover, the diameter variation of the linear pores is almost as low as the diameter variation of the carbon fibers. This suggests a potential control over the size and uniformity of the linear pore dimensions by tuning the dimensions of the carbon fibers. Lastly, the significantly low diameter variation of the carbon fibers signifies that the UCF are uniform and an ideal material for producing defined uniform linear pores.
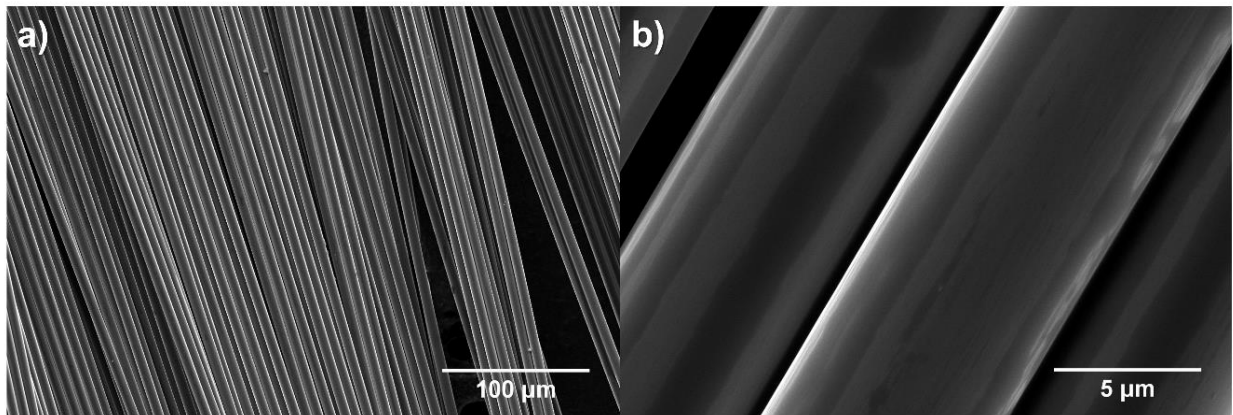
Figure 12. Scanning electron microscopy images of unidirectional carbon fiber bundles at: a) 1k and b) 20k magnification.
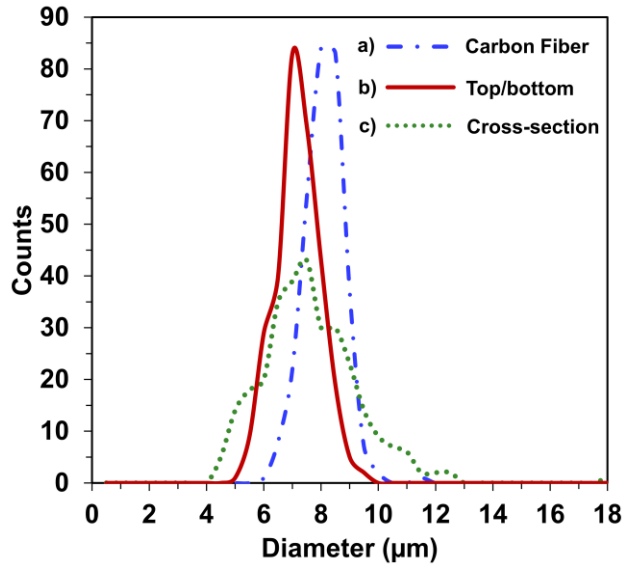
Figure 13. Distribution of diameters of: a) unidirectional carbon fiber bundles, b) continuous linear pores at the top/bottom surface of the sample, and c) continuous linear pores in the cross-sectioned sample from SEM images.

Table 3. List of mean, median, mode, and coefficient of variation of diameter distribution of CLPs on a top surface, and a cross-sectioned surface of a sample, and unidirectional carbon fibers

	Mean	Median	Mode	CV
CLPs on a top surface of a sample	7.4 µm	7.5 µm	7.5 µm	22.97
CLPs on a cross-sectioned surface of a sample	6.9 µm	7 µm	7 µm	11.35
Unidirectional carbon fiber	7.9 µm	8 µm	8 µm	8.78

The diameters of the linear pores from the top view are 6.3% smaller than the diameters of the carbon fibers; the diameters of the linear pores from the side view are 13.7% smaller than the

diameters of the carbon fibers. The diameters of the linear pores are smaller than the diameters of the carbon fibers because of pore shrinkage during sintering at 1200 ℃ for 2 hours [27]. Pore shrinkage during the densification process of sintering occurs when the decrease in pore surface energy is greater than the surface energy for grain boundary growth; the thermodynamic relation can be represented in the equation [55]:

$$N < \frac{2\pi\gamma_{sv}}{\gamma_{gb}}$$

N is the pore coordination number or number of particles around the pore, γ_{sv} is the specific surface energy of the pore and γ_{gb} is the specific grain boundary energy. In the case of the continuous linear pore, the pore coordination number is very large because there are a lot of particles around the linear pore. Therefore, the specific energy of the pore must be immense compared to the specific grain boundary energy.

3.1.2 Morphological comparison to other studies

Many studies have also researched different methods of tuning the porous structures to improve transport; similarly, all tuning focuses on orienting the pores to be perpendicular to the inlet surface and shaping the pores to have low tortuosity. For example, as seen in figure 14, Pan et al. constructed SOFC samples with aligned pore structures that were a result of the percolation of small increments of rod-like pores and oriented perpendicular to the inlet surface [40]. Similarly, Kang et al. used a multi-step sacrificial template made of anodic alumina oxide (AAO) to fabricate aligned and continuous nanosized functionally graded pores [56]. Chen et al. fabricated an anode substrate with long-shard like porous structures using a freeze tape casting method; it exhibited a

minimum tortuosity factor of 1.3 or tortuosity of 1.14 [11]. Likewise, Lichtner et al. created a cathode with aligned macro pore channels using a freeze-casting method; it had a minimum tortuosity of around 2 [57]. Yoon et al. used laser ablation to create a uniform array of cone-shaped, micron-sized pores oriented perpendicular to the inlet surface [41]. As seen in figure 14 and table 4, the multistage templating method employed by Kang et al. and the laser ablation method of Yoon et al. are costly because of AAO material cost and laser processing cost, respectively. The only low-cost methods are freeze-casting, pore forming with paper fibers, and sacrificial templating with unidirectional carbon fibers. Unidirectional carbon fibers sacrificial templating method is the only low-cost method that produces pores that are continuous from inlet to electrolyte surface, micron sized, and is uniform in size and shape.
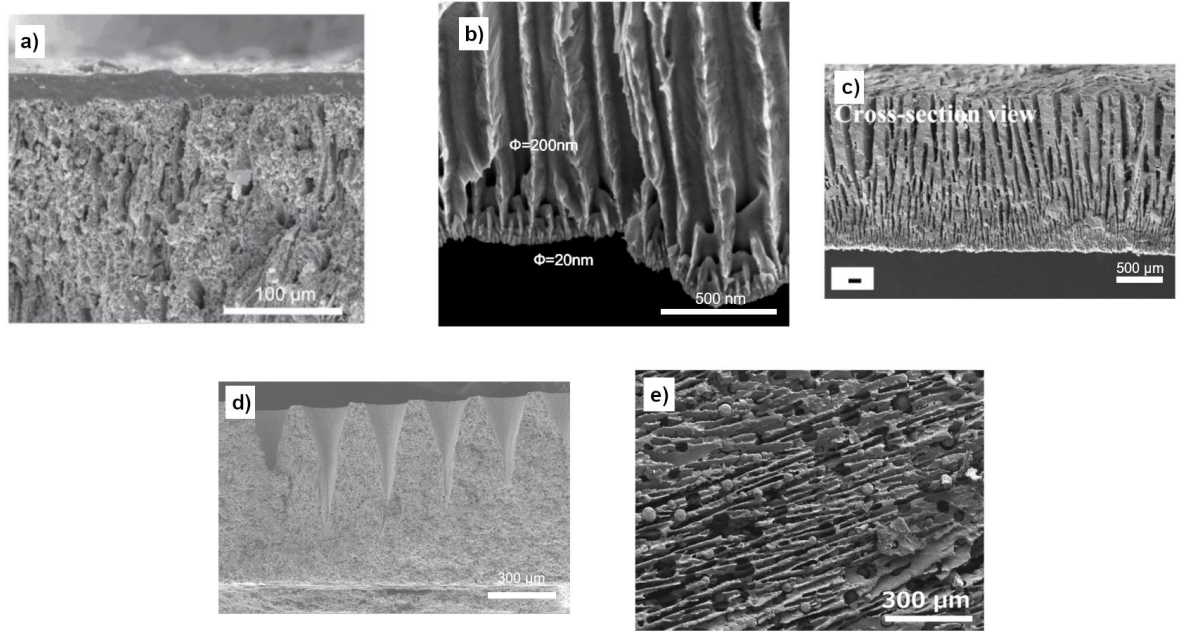
Figure 14. SEM images of pore morphologies in SOFC electrodes created by: a) Pan et al. paper fiber pore forming method, b) Kang et al. AAO sacrificial templating method, c) Chen et al. freeze-casting method, d) Yoon et al. laser ablation method, and e) Litchner et al. freeze-casting method.

Table 4. List for a comparison of perpendicular linear pore structures from other literature

Method	Diameter of linear Pores	Shape of linear pores	Shape Uniformity	Uniform Size	Continuous from Inlet to Electrolyte Surface	Cost
Paper fiber pore forming [40]	5 µm	Percolation of small segments of cylindrical pores	No	No	Yes	Low
Freeze casting [42, 57]	10-100 µm	Functionally graded shard-like pores (tortuous at one end)	No	No	Yes	Low
Multistage AAO templating [56]	20-200 nm	Rectangular shaped channels with a 1 µm layer of graded pores (tortuous at one end)	No	Yes	Yes	High
Laser ablation [41]	-225 µm	Up-side down Cone shape	Yes	Yes	No	High
Sacrificial templating using unidirectional carbon fibers	7-7.4 µm	Cylindrical shape	Yes	Yes	Yes	Low

3.2 UCF decomposition and crystal structure analysis

The XRD analysis in figure 14 confirms that a) the carbon fibers used is amorphous because of its broad peak of the (002) at $2\theta = 25.9$ º and its absence of the peak of (004) [58]. This indicates that the surface of the carbon fibers used have functional groups on its surface such as hydroxyl, carboxyl, and amine groups. This suggests that the surface is hydrophilic and does not require further surface treatments to have a good dispersion of carbon fibers in the water-based

39

NiO-YSZ slurry during slip casting [59]. And, the other two XRD patterns show the existence of a) the YSZ cubic phase at $2\theta = 30.2, 35.0, 50.3, 59.7, 73.8, 79.5, 81.7$, and 84.3 º and b) NiO cubic phase at $2\theta = 37.4, 43.5, 63.0, 75.5$ º [60, 61]. This suggests that sintering at 1200 ℃ with a 2-hour holding time at 5 ℃/min is enough to densify the green body with no phase changes of NiO and YSZ. The XRD also confirms, when comparing the XRD patterns of the sintered Ni-YSZ anode with the carbon fiber, the broad (002) peak at $2\theta = 25.9$ º is not shown in the sintered plate XRD plot. This result indicates that there is no carbon source because of the complete thermal decomposition of carbon fibers. On top of this, in figure 15, the TGA curve of the pristine carbon fibers also confirms the complete thermal decomposition at 1000 ℃ in air atmosphere at a heating rate of 5 ℃/min. This result suggests that the carbon fibers have been fully decomposed before the Ni-YSZ has fully sintered. Nevertheless, the shape of the carbon fibers is maintained in the form of CLPs after complete thermal decomposition of the carbon fibers. Conclusively, the complete decomposition of carbon fibers from TGA and XRD results proves that carbon fibers we used are effective sacrificial templates for the fabrication of defined CLPs and does not leave carbon sources in the sintered anode.
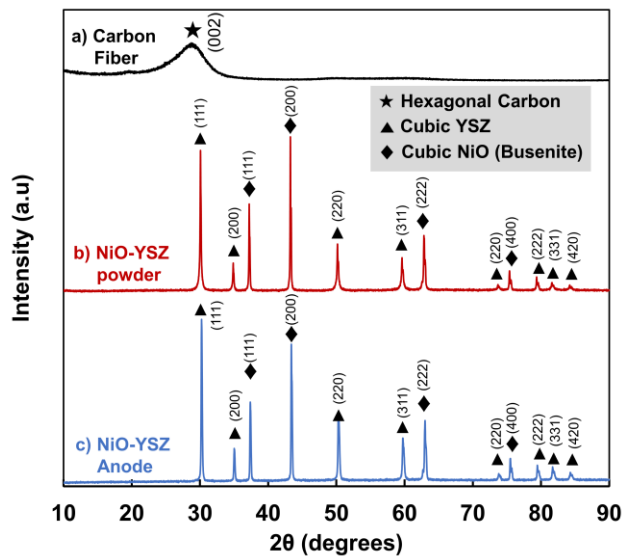
Figure 15. X-ray diffraction patterns of a) raw unidirectional carbon fiber bundles, b) NiO-YSZ powders, and c) a sintered NiO-YSZ anode.
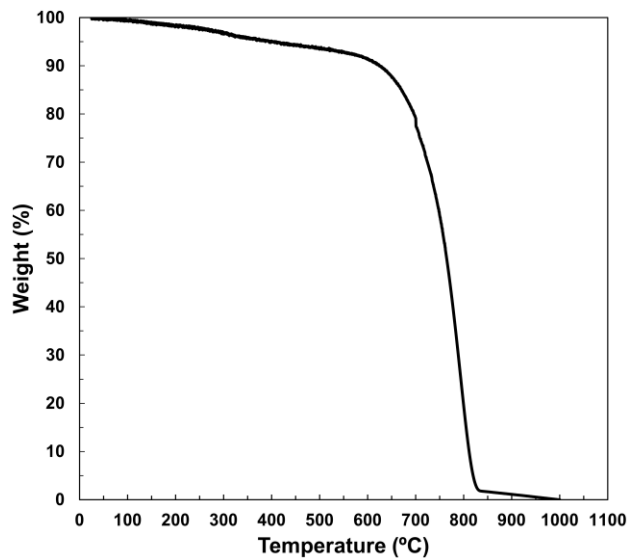
Figure 16. Thermogravimetric analysis of raw unidirectional carbon fibers under air atmosphere with a heating rate of 5 ºC/min.

41

3.3. Potential effects: Increase in open pores

The figures 16 a) and c) illustrate a traditional porous Ni-YSZ and a porous Ni-YSZ with CLPs before the first operation, respectively, from the cross-sectional analysis. And, the figures 16 b) and d) depict a possible scenario of a traditional porous Ni-YSZ and a porous Ni-YSZ with CLPs. The traditional porous Ni-YSZ contains both open pores and closed pores as depicted in figure 16 b). Open pores are the pore network that is connected from the top inlet surface to the bottom electrolyte surface; this pore network is used to facilitate mass transport of hydrogen gas and steam. Closed pores are isolated from the pore network and disallows mass transport. Figure 16 c) shows the morphology of CLPs in the anode which are derived from the SEM analysis. Figure 16 d) highlights there are much less closed pores in the anode system with CLPs because the existence of CLPs would increase number of open pores in the system, compared to the traditional porous anode.
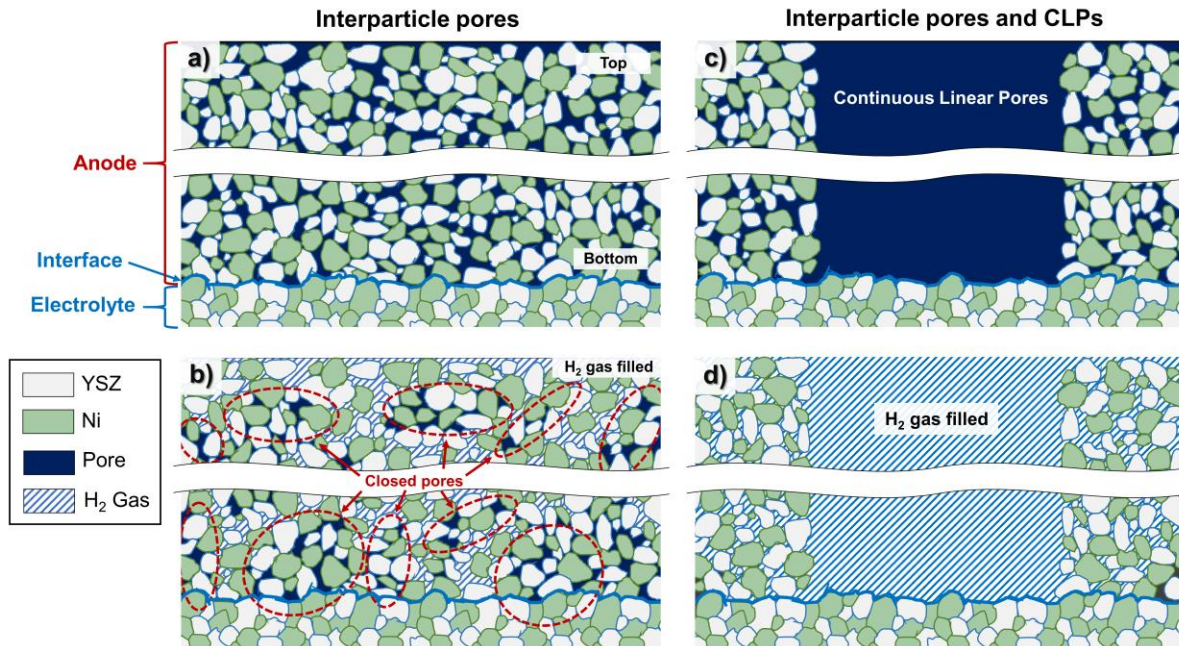
Figure 17. Schematic morphologies of a) a traditional porous Ni-YSZ before the first operation, b) during operation, c) a porous Ni-YSZ with micro-scaled continuous linear pores before the first operation, d) during operation.

3.4.1 Elemental mapping analysis

Figures 17 a) and b) are the EDS mapping images of the top surface and cross-sectioned view of the sample; it reveals the dispersion of the NiO and YSZ phases. Evidently, each elemental map depicts a good dispersion of each element. This suggests that the NiO and YSZ phases are not clustered and have a good distribution, resulting in a good percolation of both phases [15, 62]. Therefore, a good percolation creates more pathways for oxygen ions and electrons to travel to and from active TPB sites. TPB sites are only considered active when its YSZ phase is in

43

connection with YSZ phases that are connected to the electrolyte, and its Ni phase is in connection

with Ni phases that lead up to the current collector on the inlet surface.
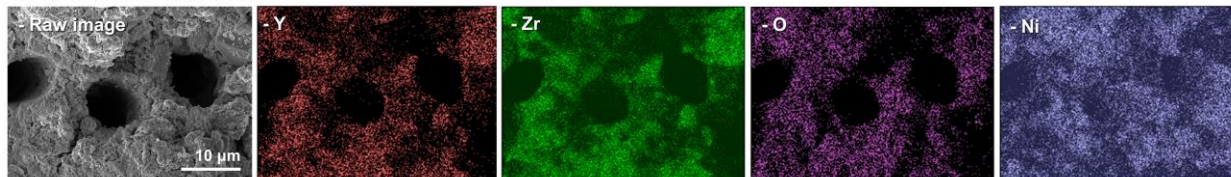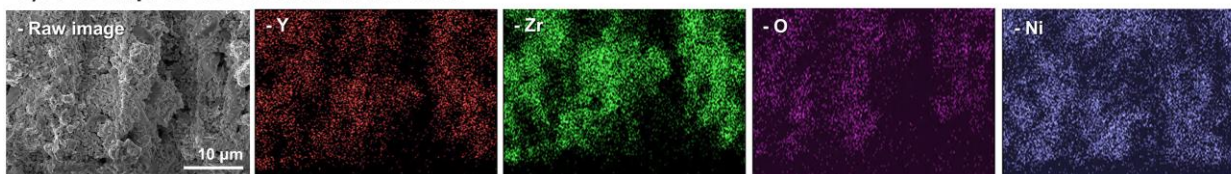
Figure 18. Energy-dispersive x-ray spectroscopy maps of a) top surface and b) cross-sectioned side of a porous NiO-YSZ with continuous linear pores: raw images, Y (red), Zr (green), O (magenta), and Ni (blue).

3.4.2 Potential Effects: Increase in Active TPBs

Figures 18 a) and b) depict a comparison of numbers of active TPB and inactive TPB sites in a traditional porous anode and a porous anode with micro-scaled continuous linear pores. Red dots indicate active TPB sites in open pores and yellow-filled dots inactive TPB sites in closed pores. All TPB sites refer to the interface between any pores, a Ni phase, and a YSZ phase. The interparticle pore phases are assumed to have the same dispersion and percolation in both cases. In figure 18 a), a traditional porous anode system contains nano-sized interparticle pores. And, those pores are categorized into open pores and closed pores according to whether the pores are connected or not. Thus, the TPBs inside of the closed pores are inactive TPBs. In contrast, as

44

depicted in figure 18 b), the existence of micro-scaled CLPs is expected to increase the existence of open pores inside of an anode. Thus, there is a greater number of active TPBs in a porous anode with CLPs, resulting in an increase in the performance of SOFC.
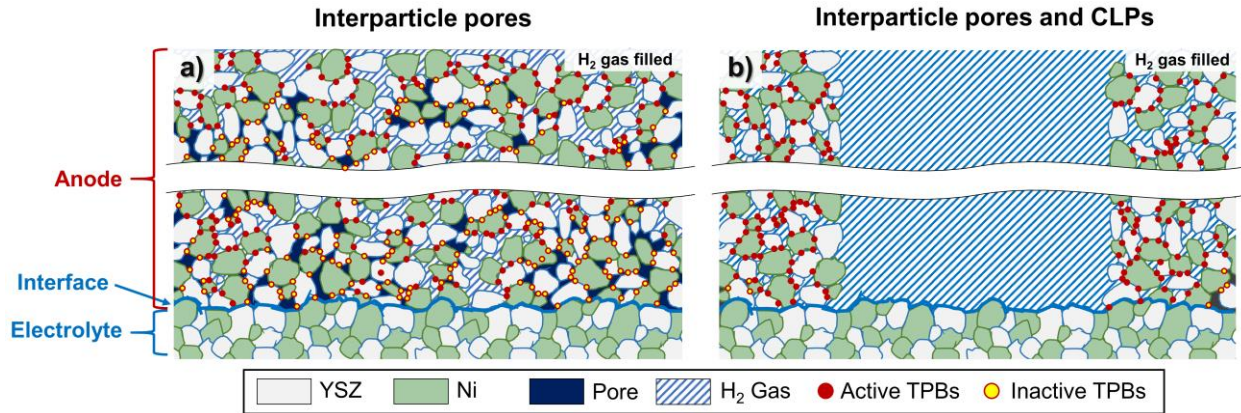
Figure 19. Schematic comparison of numbers of active TPB and inactive TPB sites in a) a traditional porous anode and b) a porous anode with micro-scaled continuous linear pores. Red dots indicate active TPB sites and yellow-filled dots inactive TPB sites.

In figure 19, the EDS mapping images supports this discussion. Figure 19 a) is an elemental mapping of the top view of the anode with CLPs and the black circles represent the top view of the CLPs. Also, because the CLPs are open pores, any interface between the Ni phase and the YSZ phase on the border of a CLP is considered an active TPB site. Evidently, there is a high concentration of active TPB sites around the border of the CLP. Figure 19 b) depicts the elemental mapping for the side view of the CLPs and the walls that are between each CLP. All areas within the inner walls of the CLPs are considered open-pore phase. Therefore, all interfaces between the NiO phase (purple) and the YSZ phase (green) on the inner walls of the linear pores are considered

active TPB sites. And, the inner walls are connected to nano-scaled open pores inside of the wall

between micro-scaled TPBs. This suggests that the existence of CLPs reduces the number of closed

pores in the porous anode and increases the active TPBs in that system. Conclusively, the

combination of nano-sized pores and micro-scaled CLPs increases numbers of active TPBs,

resulting in an increase in the performance of SOFC. Furthermore, because the amount and size of

the linear pores can be tuned by changing the amount and the diameters of carbon fiber templates,

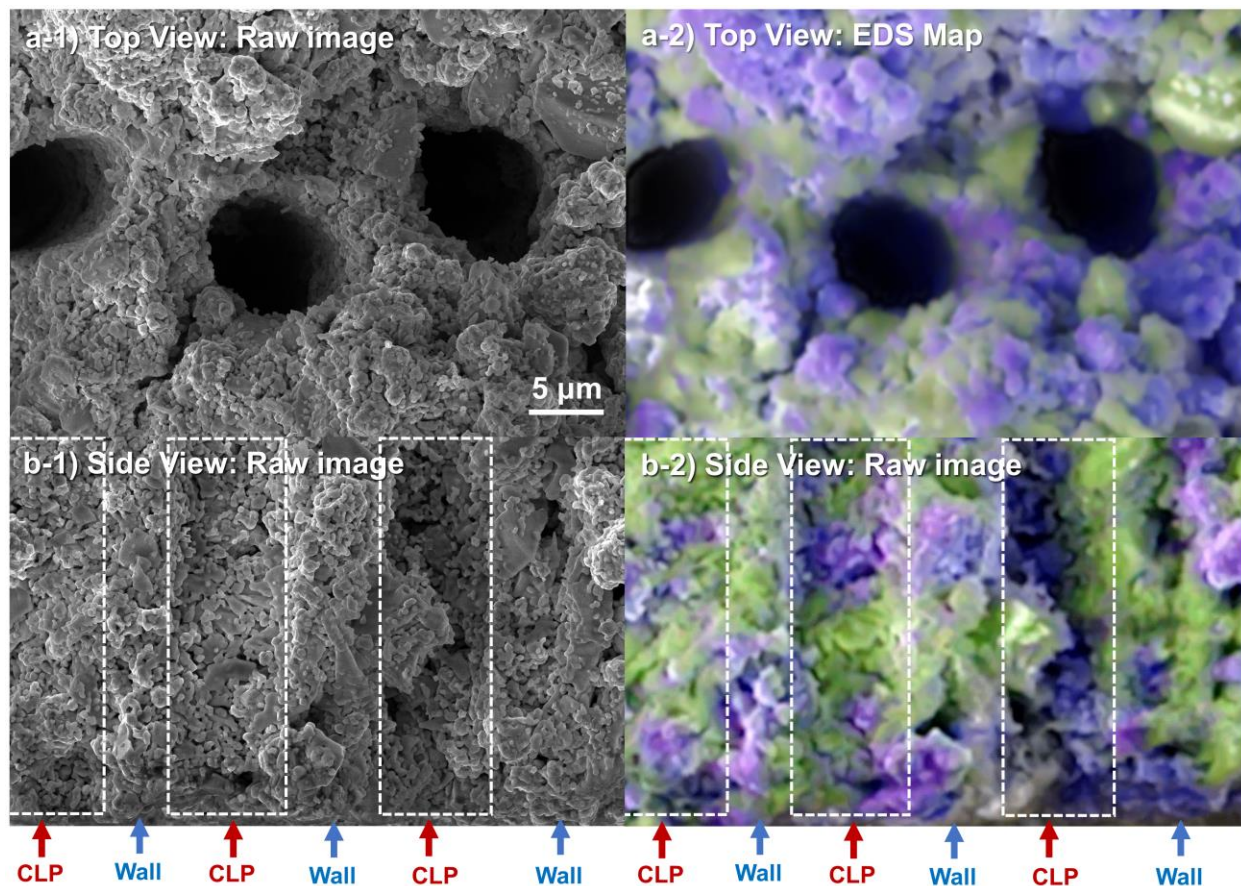there is a possibility that the numbers of TPB sites can also be controlled.

Figure 20. a-1) An SEM image of top view of a porous NiO-YSZ with micro-scaled CLPs, a-2)

an overlapped EDS mapping image on a-1), b-1) an SEM image of cross-sectioned side view of a

porous NiO-YSZ with micro-scaled CLPs, and b-2) an overlapped EDS mapping image on b-1). Purple is the NiO phase, green is the YSZ phase, black in a-1) and a-2) is the pore phase.

3.5 Potential Effects: Mass Transport Improvement

As seen in figure 20 a), the pore system in the anode with only interparticle pores renders the mass transport of steam out of the system inefficient because of an increased mean free path of steam molecules and Knudsen effect. The highly tortuous pore passages increase the mean free path of H_2O gas molecules inside of nano-sized pores because they frequently bounce with walls of the narrow pores as well as the other gas molecules. Therefore, the H_2O vapor molecules in the pore channels that are narrower than 100 nm experiences a bottle neck for mass transport because of Knudsen diffusion. This inefficient transport of steam is one of the major problems of the current SOFC system because accumulated steam molecules decrease the overall concentration of H_2 gas inside of the anode. As a result, less reaction occurs at TPB sites of the anode [37]. Moreover, steam can also react with the Ni, create undesirable Ni phases that cause Ni to agglomerate, cause degradation in the Ni-YSZ, and further decrease SOFC performance [37, 63]. As depicted in figure 20 b), the existence of the micro-scaled CLP decreases the mean free path and Knudsen diffusion of steam molecules, provides the most efficient path for the mass transport of steam, and retains the high concentration of H_2 gas molecules even near at the interface between the anode and the electrolyte. Therefore, the vector sum of mass transport of steam upwards towards the exit surface in the anode with both interparticle pores and CLPs is considerably greater than that of in the anode with only interparticle pores.

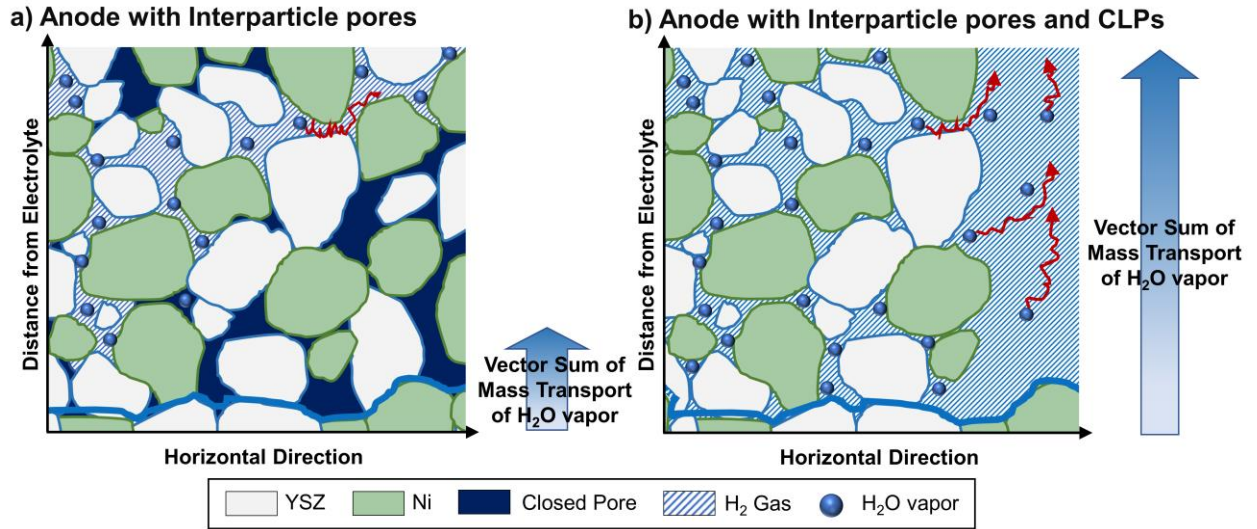**Figure 21.** Scheme for mass transport behaviors of produced steam at active TPBs inside of a) an anode only with interparticle pores and b) an anode with interparticle pores and CLPs.

Chapter 2, 3, and 4 are currently being prepared for submission for publication of the material. Cheung, Carson; Choi, Seongcheol; Graeve, Olivia A. The thesis author was the primary investigator and author of this material.

Chapter 4

Conclusions and Future Works

The structure of micro-scaled continuous linear pores and nano-sized interparticle pores were successfully fabricated in a NiO-YSZ anode by using complete thermal decomposition of embedded unidirectional carbon fiber bundles during sintering. The uniform CLP with a mean pore diameter of 7 µm (CV: 11.35) and a mean tortuosity value of 1.003 (CV: 0.59) were achieved. Moreover, the diameter, and density of the CLP can be controlled by changing the size and the amount of carbon fibers inside of the green body. Furthermore, it was confirmed that the carbon fibers are a quality candidate because it decomposes well before the NiO-YSZ sintering temperature, but it still molds high quality CLP and does not affect the crystal structure of the NiO-YSZ. It was also discussed that the CLP has potential effects that increase numbers of open pores, increase the active TPB sites, and improved gas transport. Conclusively, by using a porous NiO-YSZ with CLP structure, it is expected to drastically increase the performance of SOFC in the future work.

Future works will consist of the experimentation of a method to evenly distribute CLPs throughout the NiO-YSZ anode. It imperative to first promote the dispersion of the UCFs in order to eliminate any agglomeration of CLPs throughout the whole NiO-YSZ anode. The dispersion of UCFs can be achieved by immersing them in an aqueous solution with a hydrophilic dispersing agent, such as a cellulose nano crystal-PVA mixture [64] The cellulose nano crystals imparts a negative charge to the surface of the carbon fibers and causes repulsion to occur between coated carbon fibers. The PVA will promote the hydrophilicity of the carbon fibers. Also, by creating more slits in the silicone rubber and depositing more UCF arrays into the silicone rubber, the

distribution of the carbon fibers is increased. As a result of dispersing and increasing the distribution of the UCFs, an even distribution of CLPs throughout the NiO-YSZ anode can be achieved.

After the fabrication of a NiO-YSZ anode with an even distribution of CLPs, an LSM cathode will also be molded using the novel sacrificial templating method. Building linear pores in the cathode is especially important because concentration overpotentials are significantly higher than that of the anode. The high overpotential is because the composition of oxygen in air is only 21% [37, 65]. Therefore, larger pressures of air need to be supplied into the cathode in order to reach the TPBs closest to the cathode-electrolyte surface and maximize the usage of all TPBs in the cathode. When this phenomenon is combined with the high tortuosity problem in traditional electrodes, the concentration overpotential is considerably increased. Figure 21 depicts how the cathodic concentration overpotential dramatically increases with increasing current density, while the anodic concentration overpotential remains constant [65]. In other words, to produce a higher current density a higher concentration of air or higher pressure of air is needed. The alternative to this solution is to decrease the cathode thickness or to significantly increase the effective diffusion coefficient [37, 65]. Therefore, by constructing CLPs with low tortuosity in the cathode, the concentration gradient between the surface and the cathode-electrolyte interface will be minimized and the rate of oxygen transport to all TPBs will be maximized.
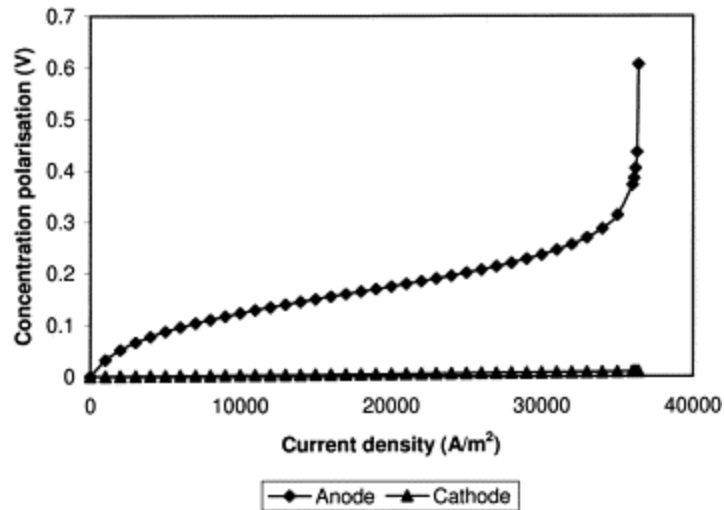
Figure 22. Trend of concentration overpotential vs current density for both anode and cathode [65].

Performance analysis of an SOFC with electrodes with both CLPs and interparticle pores will then be conducted along with a baseline SOFC with no linear pores in both electrodes. The two types of performance analysis typically done for SOFC's are current-voltage (j-v) characterization and electrochemical impedance spectroscopy (EIS). j-v characterization summarizes the electrical output with respect to general electrochemical parameters [66]. Power density and current density with respect to temperature and flow rates can easily be analyzed using this method. EIS is used to investigate the impedance or overpotential that is producing resistance for the SOFC's electrochemical performance [66].

Chapter 2, 3, and 4 are currently being prepared for submission for publication of the material. Cheung, Carson; Choi, Seongcheol; Graeve, Olivia A. The thesis author was the primary investigator and author of this material.

References

[1] R.M. Ormerod, Solid oxide fuel cells, Chemical Society Reviews. 32 (2002) 17–28. https://doi.org/10.1039/b105764m.

[2] M. Turco, A. Ausiello, L. Micoli, Fuel Cells Operating and Structural Features of MCFCs and SOFCs, in: Treatment of Biogas for Feeding High Temperature Fuel Cells, Springer International Publishing, 2016: pp. 31–76. https://doi.org/10.1007/978-3-319-03215-3_2.

[3] O'Hayre, R., Cha, S.-W., Colella, W., & Prinz, F. B. (2016). Fuel Cell Fundamentals. John Wiley & Sons, Inc. https://doi.org/10.1002/9781119191766.

[4] V.M. Janardhanan, O. Deutschmann, Modeling of Solid-Oxide Fuel Cells, Zeitschrift Für Physikalische Chemie. 221 (2007) 443–478. https://doi.org/10.1524/zpch.2007.221.4.443.

[5] A.B. Stambouli, E. Traversa, Solid oxide fuel cells (SOFCs): a review of an environmentally clean and efficient source of energy, Renewable and Sustainable Energy Reviews. 6 (2002) 433–455. https://doi.org/10.1016/s1364-0321(02)00014-x.

[6] L. Chick, M. Weimar, G. Whyatt, M. Powell, The Case for Natural Gas Fueled Solid Oxide Fuel Cell Power Systems for Distributed Generation, Fuel Cells. 15 (2014) 49–60. https://doi.org/10.1002/fuce.201400103.

[7] S. Singhal, K. Kendall, High Temperature and Solid Oxide Fuel Cells. (2003). Elsevier. https://doi.org/10.1016/b978-1-85617-387-2.x5016-8.

[8] S.J. Cooper, N.P. Brandon, An Introduction to Solid Oxide Fuel Cell Materials, Technology and Applications, in: Solid Oxide Fuel Cell Lifetime and Reliability, Elsevier, 2017: pp. 1–18. https://doi.org/10.1016/b978-0-08-101102-7.00001-5.

[9] C. Zuo, M. Liu, M. Liu, Solid Oxide Fuel Cells, in: Sol-Gel Processing for Conventional and Alternative Energy, Springer US, 2012: pp. 7–36. https://doi.org/10.1007/978-1-4614-1957-0_2.

[10] Ni, M., & Zhao, T. S. (Eds.). (2013). Solid Oxide Fuel Cells. Energy and Environment Series. Royal Society of Chemistry. https://doi.org/10.1039/9781849737777.

[11] J. Fergus, R. Hui, X. Li, D. Wilkinson, J. Zhang, Solid Oxide Fuel Cells Materials Properties Book, CRC Press, Florida, 2009.

[12] Hartmanová, M. (2003). Russian Journal of Electrochemistry, 39(5), 478–486. https://doi.org/10.1023/a:1023864524128.

[13] Park, J., Kim, D., Baek, J., Yoon, Y.-J., Su, P.-C., & Lee, S. (2018). Effect of Electrolyte Thickness on Electrochemical Reactions and Thermo-Fluidic Characteristics inside a SOFC Unit Cell. Energies, 11(3), 473. https://doi.org/10.3390/en11030473.

[14] Kaur, G. (2016). Solid Oxide Fuel Cell Components. Springer International Publishing. https://doi.org/10.1007/978-3-319-25598-9.

[15] Lu, X., Heenan, T. M. M., Bailey, J. J., Li, T., Li, K., Brett, D. J. L., & Shearing, P. R. (2017). Correlation between triple phase boundary and the microstructure of Solid Oxide Fuel Cell anodes: The role of composition, porosity and Ni densification. Journal of Power Sources, 365, 210–219. https://doi.org/10.1016/j.jpowsour.2017.08.095.

[16] D. Richerson, Modern Ceramic Engineering Book, third ed., CRC Press, Florida, 2009.

[17] Ferreira, J. M. F. (1998). Role of the clogging effect in the slip casting process. Journal of the European Ceramic Society, 18(9), 1161–1169. https://doi.org/10.1016/s0955-2219(98)00038-7.

[18] L.A. Lyon, Handbook of Applied Surface and Colloid Chemistry. Volumes 1 and 2 Edited by Krister Holmberg (Chalmers University of Technology). John Wiley & Sons: West Sussex. 2002. xii + 1110 pp. $600.00. ISBN 0-471-49083-0., Journal of the American Chemical Society. 124 (2002) 15143–15144. https://doi.org/10.1021/ja025281k.

[19] Kakade, M. B., Das, D., & Ramanathan, S. (2011). Studies on slip casting behavior of lanthanum strontium manganite. Ceramics International, 37(6), 1789–1793. https://doi.org/10.1016/j.ceramint.2011.01.044.

[20] Chou, K.-S., & Lee, L.-J. (1989). Effect of Dispersants on the Rheological Properties and Slip Casting of Concentrated Alumina Slurry. Journal of the American Ceramic Society, 72(9), 1622–1627. https://doi.org/10.1111/j.1151-2916.1989.tb06293.x.

[21] Ishikawa, Y., Katoh, Y., & Ohshima, H. (2005). Colloidal stability of aqueous polymeric dispersions: Effect of pH and salt concentration. Colloids and Surfaces B: Biointerfaces, 42(1), 53–58. https://doi.org/10.1016/j.colsurfb.2005.01.006.

[22] Tseng, W. J., & Chen, C.-N. (2003). Effect of polymeric dispersant on rheological behavior of nickel–terpineol suspensions. Materials Science and Engineering: A, 347(1–2), 145–153. https://doi.org/10.1016/s0921-5093(02)00562-2.

[23] Xu, Q., Gabbitas, B., Matthews, S., & Zhang, D. (2014). The Effect of Binder and Plasticizer on Porous Titanium Compacts Prepared by Slip Casting. Procedia Materials Science, 4, 81–84. https://doi.org/10.1016/j.mspro.2014.07.601.

[24] German, R. M. (2016). Sintering Trajectories: Description on How Density, Surface Area, and Grain Size Change. JOM, 68(3), 878–884. https://doi.org/10.1007/s11837-015-1795-8.

[25] DEJONGHE, L., & RAHAMAN, M. (2003). 4.1 Sintering of Ceramics. In Handbook of Advanced Ceramics (pp. 187–264). Elsevier. https://doi.org/10.1016/b978-012654640-8/50006-7.

[26] Corbin, S. F., & Apté, P. S. (1999). Engineered Porosity via Tape Casting, Lamination and the Percolation of Pyrolyzable Particulates. Journal of the American Ceramic Society, 82(7), 1693–1701. https://doi.org/10.1111/j.1151-2916.1999.tb01988.x.

[27] Sarikaya, A., & Dogan, F. (2013). Effect of various pore formers on the microstructural development of tape-cast porous ceramics. Ceramics International, 39(1), 403–413. https://doi.org/10.1016/j.ceramint.2012.06.041.

[28] Agarwal, B., Broutman, L. & Chandrashekhara, K, Analysis and Performance of Fiber Composites, fourth ed., John Wiley & Sons, New Jersey, 2017.

[29] Tranchard, P., Duquesne, S., Samyn, F., Estèbe, B., & Bourbigot, S. (2017). Kinetic analysis of the thermal decomposition of a carbon fibre-reinforced epoxy resin laminate. Journal of Analytical and Applied Pyrolysis, 126, 14–21. https://doi.org/10.1016/j.jaap.2017.07.002.

[30] Fahlman, B. D. (2011). Materials Characterization. In Materials Chemistry (pp. 585–667). Springer Netherlands. https://doi.org/10.1007/978-94-007-0693-4_7.

[31] D. Shindo, T. Oikawa, Analytical Electron Microscopy for Materials Science, Springer Japan, 2002.

[32] M. De Graef, M. E. McHenry, Structure of Materials Book, second ed., Cambridge University, United Kingdom, 2012.

[33] Vyazovkin, S. (2012). Thermogravimetric Analysis. Characterization of Materials. John Wiley & Sons, Inc. https://doi.org/10.1002/0471266965.com029.pub2.

[34] R. O'Hayre, S. Cha, W. Colella, F. Prinz, Chapter 3: Fuel Cell Reaction Kinetics. Fuel Cell Fundamentals, John Wiley & Sons, Inc, California, 2016, pp. 77–116.

[35] Y. Shi, N. Cai, C. Li, Numerical modeling of an anode-supported SOFC button cell considering anodic surface diffusion, Journal of Power Sources. 164 (2007) 639–648. https://doi.org/10.1016/j.jpowsour.2006.10.091.

[36] B. Ghanbarian, A.G. Hunt, R.P. Ewing, M. Sahimi, Tortuosity in Porous Media: A Critical Review, Soil Science Society of America Journal. 77 (2013) 1461. https://doi.org/10.2136/sssaj2012.0435.

[37] R. O'Hayre, S. Cha, W. Colella, F. Prinz, Chapter 5: Fuel Cell Mass Transport, in: Fuel CellFundamentals, John Wiley & Sons, Inc, California, 2016: pp. 167–202.

[38] J. Zhao, J. Yao, M. Zhang, L. Zhang, Y. Yang, H. Sun, S. An, A. Li, Study of Gas Flow Characteristics in Tight Porous Media with a Microscale Lattice Boltzmann Model, Scientific Reports. 6 (2016). https://doi.org/10.1038/srep32393.

[39] W. He, W. Lv, J.H. Dickerson, Gas Diffusion Mechanisms and Models, in: Gas Transport in Solid Oxide Fuel Cells, Springer International Publishing, New York, 2014: pp. 9–17.

[40] W.-P. Pan, Z. Lü, K.-F. Chen, Y.-H. Zhang, B. Wei, Z.-H. Wang, W.-H. Su, Enhanced Performance of Solid Oxide Fuel Cell by Manipulating the Orientation of Cylindrical Pores in Anode Substrate, Fuel Cells. 12 (2012) 41–46. https://doi.org/10.1002/fuce.201100121.

[41] C. Yoon, M. Liu, D. Yuan, R. Guo, M. Liu, S. Das, Microarchitectured solid oxide fuel cells with improved energy efficiency (Part II): Fabrication and characterization, Journal of Power Sources. 293 (2015) 883–891.

[42] Y. Chen, Y. Zhang, J. Baker, P. Majumdar, Z. Yang, M. Han, F. Chen, Hierarchically Oriented Macroporous Anode-Supported Solid Oxide Fuel Cell with Thin Ceria Electrolyte Film, ACS Applied Materials & Interfaces. 6 (2014) 5130–5136. https://doi.org/10.1021/am5003662.

[43] Brus, G., Miyawaki, K., Iwai, H., Saito, M., & Yoshida, H. (2014). Tortuosity of an SOFC anode estimated from saturation currents and a mass transport model in comparison with a real micro-structure. Solid State Ionics, 265, 13–21. https://doi.org/10.1016/j.ssi.2014.07.002.

[44] C. Yoon, Computational Design, Fabrication and Characterization of Microarchitectured Solid Oxide Fuel Cells with Improved Energy Efficiency, Dissertation, Georgia Institute of Technology, Georgia, 2010.

[45] Y.B. Kim, C.-M. Hsu, S.T. Connor, T.M. Gür, Y. Cui, F.B. Prinz, Nanopore Patterned Pt Array Electrodes for Triple Phase Boundary Study in Low Temperature SOFC, Journal of The Electrochemical Society. 157 (2010) B1269. https://doi.org/10.1149/1.3455046.

[46] S. Kang, P.C. Su, Y.I. Park, Y. Saito, F.B. Prinz, Thin-Film Solid Oxide Fuel Cells on Porous Nickel Substrates with Multistage Nanohole Array, Journal of The Electrochemical Society. 153 (2006) A554. https://doi.org/10.1149/1.2164769.

[47] D. Yang, W. Zhang, R.L. Yao, B.Z. Jiang, Thermal Degradation Characteristics and Kinetics of High Temperature Vulcanized (HTV) Silicone Rubber/POSS Hybrid, Applied Mechanics and Materials. 105–107 (2011) 1657–1661. https://doi.org/10.4028/www.scientific.net/amm.105-107.1657.

[48] I. Gonzalo-Juan, B. Ferrari, M.T. Colomer, A.J. Sánchez-Herencia, Colloidal processing and sintering of porous percolative Ni-YSZ layers, Journal of Membrane Science. 352 (2010) 55–62. https://doi.org/10.1016/j.memsci.2010.01.060.

[49] L.H. Luo, Y. Lang, Z.Z. Huang, L. Cheng, J.J. Shi, Fabrication of YSZ Film by Aqueous Tape Casting Using PVA-B1070 Cobinder for IT-SOFC, Key Engineering Materials. 434–435 (2010) 735–738. https://doi.org/10.4028/www.scientific.net/kem.434-435.735.

[50] T. Fukui, S. Ohara, M. Naito, K. Nogi, Performance and stability of SOFC anode fabricated from NiO–YSZ composite particles, Journal of Power Sources. 110 (2002) 91–95. https://doi.org/10.1016/s0378-7753(02)00218-5.

[51] R.F. Martins, M.C. Brant, R.Z. Domingues, R.M. Paniago, K. Sapag, T. Matencio, Synthesis and characterization of NiO-YSZ for SOFCs, Materials Research Bulletin. 44 (2009) 451–456. https://doi.org/10.1016/j.materresbull.2008.04.017.

[52] G. Brus, K. Miyawaki, H. Iwai, M. Saito, H. Yoshida, Tortuosity of an SOFC anode estimated from saturation currents and a mass transport model in comparison with a real micro-structure, Solid State Ionics. 265 (2014) 13–21. https://doi.org/10.1016/j.ssi.2014.07.002.

[53] M. Kishimoto, H. Iwai, M. Saito, H. Yoshida, Quantitative Evaluation of Transport Properties of SOFC Porous Anode by Random Walk Process, in: ECS Transactions, ECS, Missouri, 2009.

[54] M. Kishimoto, H. Iwai, M. Saito, H. Yoshida, Quantitative evaluation of solid oxide fuel cell porous anode microstructure based on focused ion beam and scanning electron microscope technique and prediction of anode overpotentials, Journal of Power Sources. 196 (2011) 4555–4563. https://doi.org/10.1016/j.jpowsour.2010.12.100.

[55] M.N. Rahaman, Ceramic Processing and Sintering, CRC Press, Florida, 2017.

[56] S. Kang, P.C. Su, Y.I. Park, Y. Saito, F.B. Prinz, Thin-Film Solid Oxide Fuel Cells on Porous Nickel Substrates with Multistage Nanohole Array, Journal of The Electrochemical Society. 153 (2006) A554. https://doi.org/10.1149/1.2164769.

[57] A.Z. Lichtner, D. Jauffrès, D. Roussel, F. Charlot, C.L. Martin, R.K. Bordia, Dispersion, connectivity and tortuosity of hierarchical porosity composite SOFC cathodes prepared by freeze-casting, Journal of the European Ceramic Society. 35 (2015) 585–595. https://doi.org/10.1016/j.jeurceramsoc.2014.09.030.

[58] S.R. Dhakate, A. Chaudhary, A. Gupta, A.K. Pathak, B.P. Singh, K.M. Subhedar, T. Yokozeki, Excellent mechanical properties of carbon fiber semi-aligned electrospun carbon nanofiber hybrid polymer composites, RSC Advances. 6 (2016) 36715–36722. https://doi.org/10.1039/c6ra02672a.

[59] H. Kim, Y.-J. Lee, D.-C. Lee, G.-G. Park, Y. Yoo, Fabrication of the carbon paper by wet-laying of ozone-treated carbon fibers with hydrophilic functional groups, Carbon. 60 (2013) 429–436. https://doi.org/10.1016/j.carbon.2013.04.057.

[60] M.B. Kakade, S. Ramanathan, D. Das, Gel-combustion, characterization and processing of porous Ni–YSZ cermet for anodes of solid oxide fuel cells (SOFCs), Ceramics International. 37 (2011) 195–200. https://doi.org/10.1016/j.ceramint.2010.09.019.

[61] H.S. Hong, U.-S. Chae, S.-T. Choo, K.S. Lee, Microstructure and electrical conductivity of Ni/YSZ and NiO/YSZ composites for high-temperature electrolysis prepared by mechanical alloying, Journal of Power Sources. 149 (2005) 84–89. https://doi.org/10.1016/j.jpowsour.2005.01.057.

[62] B. Shri Prakash, S. Senthil Kumar, S.T. Aruna, Properties and development of Ni/YSZ as an anode material in solid oxide fuel cell: A review, Renewable and Sustainable Energy Reviews. 36 (2014) 149–179. https://doi.org/10.1016/j.rser.2014.04.043.

[63] M. Chen, Y.-L. Liu, J.J. Bentzen, W. Zhang, X. Sun, A. Hauch, Y. Tao, J.R. Bowen, P.V. Hendriksen, Microstructural Degradation of Ni/YSZ Electrodes in Solid Oxide Electrolysis Cells under High Current, Journal of The Electrochemical Society. 160 (2013) F883–F891. https://doi.org/10.1149/2.098308jes.

[64] Y. Liu, B. Sun, J. Li, D. Cheng, X. An, B. Yang, Z. He, R. Lutes, A. Khan, Y. Ni, Aqueous Dispersion of Carbon Fibers and Expanded Graphite Stabilized from the Addition of Cellulose Nanocrystals to Produce Highly Conductive Cellulose Composites, ACS Sustainable Chemistry & Engineering. 6 (2018) 3291–3298. https://doi.org/10.1021/acssuschemeng.7b03456.

[65] S.. Chan, K.. Khor, Z.. Xia, A complete polarization model of a solid oxide fuel cell and its sensitivity to the change of cell component thickness, Journal of Power Sources. 93 (2001) 130–140. https://doi.org/10.1016/s0378-7753(00)00556-5.

[66] Q.-A. Huang, R. Hui, B. Wang, J. Zhang, A review of AC impedance modeling and validation in SOFC diagnosis, Electrochimica Acta. 52 (2007) 8144–8164. https://doi.org/10.1016/j.electacta.2007.05.071.